ADAPTIVE QUASIMETRIC MAPPING : PRINCIPLED TOPOLOGICAL ABSTRACTION FOR ROBUST OFFLINE GOAL-CONDITIONED NAVIGATION

Anthony Kobanda[1,2], **Waris Radji**[2], **Odalric-Ambrym Maillard**[2], **Rémy Portelas**[1]
[1]Ubisoft La Forge, Bordeaux, France,
[2]Inria, Univ. Lille, CNRS, Centrale Lille, UMR 9198-CRIStAL, F-59000 Lille, France.

ABSTRACT

Goal-Conditioned Reinforcement Learning aims to design agents that can reach specified goals, notably from previously collected trajectories in the offline setting. In this context, graph-based learning approaches have been proposed to mitigate compounding value-estimation errors in long-horizon navigation tasks. However, existing methods typically rely on dense keypoint coverage of the dataset support, resulting in computationally expensive planning. Moreover, they lack explicit mechanisms to adapt to topological changes (e.g., new obstacles), hindering deployment in live applications such as video game environments. To address these two shortcomings, we introduce Adaptive Quasimetric Mapping (AQM), an offline framework leveraging a "time-to-reach" quasimetric learned from the available data. Crucially, it builds a sparse cover of the dataset support, as a greedy approximation to a dominating set problem. At test-time, the resulting graph is carefully pruned by comparing the observed edge traversal time against a time-to-reach budget derived from the quasimetric, thus enabling zero-shot replanning. Empirically, we evaluate AQM on navigation tasks ranging from a classical to a video-game-like benchmark evaluating adaptation across tasks. We show that AQM achieves competitive performance while requiring up to 100× fewer keypoints than prior approaches, demonstrating the relevance of topological abstraction for GCRL.

1 INTRODUCTION

Humans improve knowledge and master complex skills by iteratively exploring and refining different internal notions of proximity ("*How far am I from succeeding ?*") and progress ("*Is this action helpful ?*") (Ericsson et al., 1993). Reinforcement learning (RL) (Sutton & Barto, 2018) offers the computational analogue, combining trial-and-error with value function approximation to learn algorithms and agents that solve sequential decision problems, and is extended to high-dimensional perception planning, and control with Deep Reinforcement Learning (Arulkumaran et al., 2017).

In many real-world scenarios, active exploration is costly while vast amounts of logged interactions exist. Offline Reinforcement Learning (Offline RL) improves data efficiency by learning from pre-collected trajectories (Levine et al., 2020), but without the ability to evaluate new state-action pairs, we must optimize policies beyond the dataset's behaviour distribution (Peng et al., 2019; Kostrikov et al., 2022), a process that is sensitive to bootstrapping errors, particularly in long-horizon settings (Park et al., 2024a). Moreover, overcoming changes in the environment poses additional challenges.

By conditioning an agent's policy on a specific target, Goal-Conditioned Reinforcement Learning (GCRL) repurposes decision problems as reachability tasks (Kaelbling, 1993; Liu et al., 2022). Although Hindsight Experience Replay (Andrychowicz et al., 2017) mitigate sparse rewards and Hierarchical Policies (Li et al., 2022; Park et al., 2023) ease path planning, most fall short when tackling long-horizon navigation tasks, which is a focus of our research. Recent GCRL benchmarks such as **OGBench** (Park et al., 2025a) highlight these challenges in diverse experimental settings.

To tackle these issues, an approach is to plan through latent representations that encode reachability. Contrastive Learning algorithms (Eysenbach et al., 2022) cluster similar states but learn uncalibrated similarities, a key challenge highlighted by recent work on temporal distance functions. Quasimetric RL (Wang & Isola, 2022; Wang et al., 2023) provides such a reachability-aware distance, however resulting policies fail on complex tasks. Graph-based algorithms, such as Hilbert Representations (HILP) (Park et al., 2024b), Graph-Assisted Stitching (GAS) (Baek et al., 2025), and Projective Quasimetric Planning (ProQ) (Kobanda et al., 2025b), improve long-horizon navigation using learned distances and graphs, but are computationally inefficient, as they rely on a large number of keypoints.

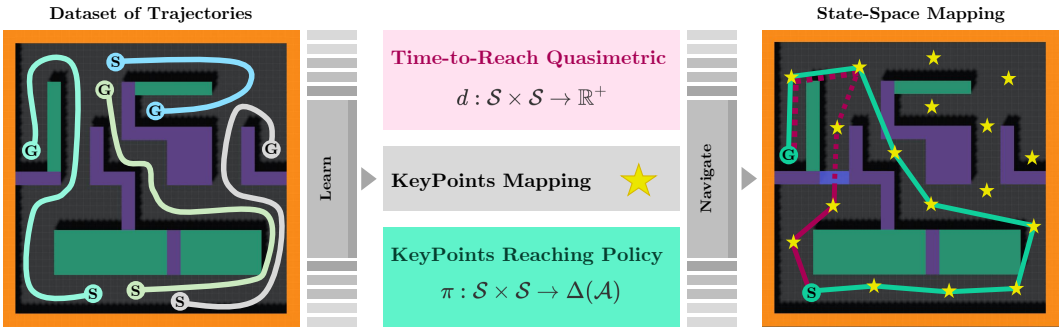

Figure 1: **Adaptive Quasimetric Mapping (AQM). (left)** We leverage $\mathcal{D} = \{\tau_i = (s_0^{(i)}, a_0^{(i)}, \ldots, s_T^{(i)})\}$ a dataset of trajectories ; **(middle)** we learn a time-to-reach quasimetric $d : \mathcal{S} \times \mathcal{S} \to \mathbb{R}^+$, a goal-conditioned policy $\pi : \mathcal{S} \times \mathcal{S} \to \Delta(\mathcal{A})$; **(right)** and the quasimetric is used to build a sparse topological graph of the state space, with keypoints (★) providing near uniform coverage of the dataset support. During inference, AQM plans a path from a starting position (S) to a goal (G) and follows it using the learned policy. It can adapt to topological changes at test-time, such as a **blocked path**, by monitoring budget overruns given predicted time-to-reach values. Consequently performing zero-shot replanning, to reach the goal through another **feasible path**.

To address these issues, we introduce a new framework : **Adaptive Quasimetric Mapping (AQM)**, thoroughly laid out in *Figure 1*. It is adaptive in the following sense: by monitoring a time-to-reach budget between keypoints during execution, an agent can infer geometric inconsistencies, trigger unreliable edges invalidation, update the initial graph, and plan new paths without having to retrain.

We argue that a bottleneck in current graph-based navigation lies in the reliance on uncalibrated distance heuristics, which dense keypoint sets to ensure connectivity. In contrast, we establish a principled approach: by learning a geometrically consistent time-to-reach quasimetric, we can extract parsimonious graphs as abstractions that are both computationally efficient and inherently adaptive.

Our main contributions are as follows :

(1) **Geometric Foundation :** We leverage a time-to-reach quasimetric function as a principled tool for topological abstraction, serving as geometric prior for both planning and control ;

(2) **Topological Abstraction :** We propose a Keypoint Selection Strategy inspired by dominating set theory yielding sparse graphs, providing a covering analysis under standard density assumptions ;

(3) **Test-Time Adaptation :** We introduce an Adaptive Planning Mechanism. By monitoring the time-to-reach, we flag inconsistencies at test-time as invalid edges, and replan alternative paths ;

(4) **Empirical Validation :** We evaluate AQM on an offline navigation benchmark, demonstrating competitive performance, while improving scalability relative to recent graph-based approaches.

While *Section 2* reviews the relevant and related literature, *Section 3* presents the necessary theoretical background contextualizing our research. In *Section 4*, we detail our approach, first going through an algorithmic overview, then we focus on on the learning process and the inference pipeline. *Section 5* presents our experimental setting, the evaluation protocol, the main results and ablation studies. We conclude in *Section 6*, notably with the limitations of our work and currently identified future work.

2 Related Work

Offline Goal-Conditioned Reinforcement Learning. In the Goal Conditioned RL framework (Kaelbling, 1993; Andrychowicz et al., 2017), states are augmented with goals, and learned policies are optimized to reach them. In the offline setting (Levine et al., 2020), policy learning must remain within the support of a given dataset, while aiming at surpassing the behavioral policy. Although value-based algorithms improve learning (Kostrikov et al., 2022), they can fail on long-horizon tasks due to approximation errors in the learned value function (Park et al., 2024a; 2025b).

Hierarchical Planning & Policy Distillation. Hierarchical approaches mitigate the aforementioned issue by planning (Li et al., 2022; Park et al., 2023) from a high-level policy, and learning actions to closer goals through a low-level one. Policy distillation methods like SAW (Zhou & Kao, 2025) compress this hierarchical structure into a flat one, offering improved stability and computational efficiency compared to two-level policies. Nevertheless, even for such methods, stitching trajectories remains difficult for long-horizon navigation tasks (Park et al., 2025a; Kobanda et al., 2025a).

Representation Learning. A key idea in order to improve performance in RL is to learn a structured latent representations (Fuest et al., 2024; Echchahed & Castro, 2025). Many approaches focus on learning behavioral similarity through self-supervised and contrastive learning objectives. Among these, CURL (Laskin et al., 2020) and CRL (Eysenbach et al., 2022) aim to map temporally close states to nearby points in a learned latent space. Other methods learn explicit latent dynamics-aware models (Gelada et al., 2019; Shi et al., 2023), aiming to capture the transition structure of the given environment. While these approaches have valuable use cases, they do not produce calibrated measure of time-to-reach between states, which we argue is a key component for principled GCRL.

Distance Learning. Value functions encode reachability but are unbounded and poorly suited as qualitative distance surrogates. This motivates explicit distance learning, where the cost-to-go induces an asymmetric notion of distance (a quasimetric). IQE (Wang & Isola, 2022) provides an expressive parameterization, and QRL (Wang et al., 2023) establishes a principled training framework for such functions. Related approaches enforce Bellman consistency, e.g., DFWRL (Dhiman et al., 2018) and TRL (Park et al., 2025c), or via TD-based distances such as MAD (Steccanella et al., 2025) ; TMD (Myers et al., 2025) combines contrastive objectives with metric-consistency losses.

Topological Abstraction. A strategy in GCRL is to build sparse mappings (Huang et al., 2019). Early methods relied on pre-computed distances and hop-based navigation, but suffered from coverage gaps or expensive nearest-neighbor search (Savinov et al., 2018; Kim et al., 2021). Recent work learns temporal distances: **ProQ** (Kobanda et al., 2025b) offers a physics-inspired planner that performs well on the settings it targets, but its OOD score depends on explicit 2D position coordinates, making extensions to higher-dimensional spaces less direct. **HILP** (Park et al., 2024b) learns a graph but can be memory-intensive since it leverages the dataset at inference. **QPHIL** (Canesse et al., 2025) discretizes but can suffer from out-of-distribution trajectory predictions. **GAS** (Baek et al., 2025) is the current state of the art, constructing a graph from filtered data to stitch trajectories while avoiding OOD subgoals, but remains computationally heavy due to dense graphs at test time.

3 PRELIMINARIES

We consider a **Markov Decision Process (MDP)** as tuple $\mathcal{M} = \big(\ \mathcal{S},\ \mathcal{A},\ \mathcal{P}_{\mathcal{S}},\ {\mathcal{P}_{\mathcal{S}}}^{(0)},\ \mathcal{R},\ \gamma\ \big)$, which provides a formal setting for RL, where $\mathcal{S}$ is a state space, $\mathcal{A}$ an action space, $\mathcal{P}_{\mathcal{S}} : \mathcal{S} \times \mathcal{A} \to \Delta(\mathcal{S})$ a transition function, ${\mathcal{P}_{\mathcal{S}}}^{(0)} \in \Delta(S)$ an initial distribution over the states, $\mathcal{R} : \mathcal{S} \times \mathcal{A} \times \mathcal{S} \to \Delta(\mathbb{R})$ a reward function, generally deterministic, and $\gamma \in]0, 1]$ a discount factor. An agent's behavior follows a policy $\pi_\theta : \mathcal{S} \to \Delta(\mathcal{A})$, parameterized by parameters $\theta \in \Theta$. In Reinforcement Learning, we aim for optimal parameters $\theta^*_{\mathcal{M}}$ maximizing the expected cumulative reward $J_{\mathcal{M}}(\theta)$.

Offline Goal-Conditioned RL (GCRL) extends the MDP to include a goal space $\mathcal{G}$, introducing ${\mathcal{P}_{\mathcal{S},\mathcal{G}}}^{(0)}$ an initial state and goal distribution, $\phi : \mathcal{S} \to \mathcal{G}$ a function mapping each state to the goal it represents, and $d : \mathcal{G} \times \mathcal{G} \to \mathbb{R}^+$ a quasimetric on $\mathcal{G}$. The policy $\pi_\theta : \mathcal{S} \times \mathcal{G} \to \Delta(\mathcal{A})$ and the reward function $\mathcal{R} : \mathcal{S} \times \mathcal{A} \times \mathcal{S} \times \mathcal{G} \to \mathbb{R}$ are now conditioned on a goal $g \in \mathcal{G}$. In our experimental setup, we consider sparse rewards allocated when the agent reaches the goal within a range $0 \leq \epsilon$: $\mathcal{R}(s_t, a_t, s_{t+1}, g) = \mathbb{1}\big(\ d(\phi(s_{t+1}), g) \leq \epsilon\ \big)$. Given a dataset of trajectories $\mathcal{D} = \big\{(s, a, r, s', g)\big\}$, the policy loss is optimized to reach the specified goals.

Unlike classical metrics, which are symmetric, GCRL value functions (or time-to-reach) functions are generally asymmetric: reaching A from B can require a different expected cost than reaching B from A. This property aligns with **Quasimetric** functions (Wilson, 1931) $d : \mathcal{G} \times \mathcal{G} \to \mathbb{R}^+$ satisfying : *Non-negativity* : $d(x, y) \geq 0$; *Identity of indiscernibles* : if $d(x, y) = 0$ then $x = y$; *Reflexivity* : $d(x, x) = 0$; *Triangle inequality* : $d(x, z) \leq d(x, y) + d(y, z)$; but not necessarily symmetry of the distance : $d(x, y) \neq d(y, x)$ (whereas **Metrics** do).

This self-consistency, defined by the triangle inequality, is the foundation for shortest-path algorithms. In the case of a finite graph, the Floyd-Warshall computes an all-pairs shortest-path quasimetric.

The Floyd-Warshall Algorithm (Floyd, 1962). Given a directed graph $G = (V, E)$ where V is a finite set of vertices and $w(i, j) \in \mathbb{R}^+ \cup \{+\infty\}$ is the weight of an edge in E from vertex i to j, the algorithm finds the shortest path quasimetric $d^*(i, j) \in \mathbb{R}^+ \cup \{+\infty\}$ between all pairs (i, j).

Proposition 3.1 (Floyd-Warshall Update)**.** *Let's consider $d_k(i, j)$ be the shortest path distance from vertex i to j using only intermediate vertices from the set $\{1, 2, \ldots, k\}$. The algorithm initializes $d_0(i, j) = w(i, j)$ and for $k = 1, \ldots, |V|$: $d_k(i, j) \leftarrow \min\big(d_{k-1}(i, j),\ d_{k-1}(i, k) + d_{k-1}(k, j)\big)$. After at most $|V|$ iterations, the $d_{|V|}$ matrix contains the true all-pairs shortest-path distances.*

4 Adaptive Quasimetric Mapping

4.1 AQM Learning Algorithm : an Overview

Algorithm 1 AQM Learning Pipeline

Require: *Dataset* $\mathcal{D} = \{(s_0^{(i)}, a_0^{(i)}, \dots, s_T^{(i)})\}$ / *Batch Size* B / *# Epochs* E / *Learning Rate* η / *Separation* δ

Initialize: Quasimetric d_θ / Lagrange Multiplier λ / Main & Target Policies π_ψ , π_{ψ^-}

Notation: s_i , s_i' a state and an immediate next state / a_i an action performed at s_i leading to s_i'

Notation: w_i a subgoal at a fixed timestep distance / g a goal sampled from some distribution

for $t = 1$ to E **do**
  Sample batch : $\{(s_i, a_i, s_i', w_i, g)\}_{i=1}^{B} \sim \mathcal{D}$
  (A) Quasimetric Learning : *Section 4.2*
  Compute Distance Losses for each sample i :
  $\mathcal{L}_{\text{close}}(s_i, s_i', \theta)$ *(Eq. 3)* : Calibrates one-step transitions
  $\mathcal{L}_{\text{push}}(s_i, g, \theta)$ *(Eq. 4)* : Pushes any state and goal apart
  Update Quasimetric Parameters θ :
  $\theta \leftarrow \theta - \eta \nabla_\theta \frac{1}{B} \sum_{i=1}^{B} (\lambda \cdot \mathcal{L}_{\text{close}} + \mathcal{L}_{\text{push}})$
  Update Lagrange multiplier λ :
  $\lambda \leftarrow \lambda + \eta \nabla_\lambda (\lambda \cdot \mathcal{L}_{\text{close}})$: Adapt the penalty weight
  (B) Policy Learning : *Section 4.4*
  Update Target Parameters : $\mathcal{L}_T(s_i, s_i', w_i, \psi^-)$ *(Eq. 5)*
  Advantage Weighted Regression on the subgoal for π_{ψ^-}
  Update Main Parameters : $\mathcal{L}_M(s_i, w_i, g_i, \psi)$ *(Eq. 6)*
  Subgoal Advantage-Weighted Bootstrapping for π_ψ
end for
(C) Keypoints Selection : *Section 4.3*
Update Keypoints $\{z_k\}_{k=1}^{K}$ by solving a maximal δ-separated set problem on $\mathcal{D}$, using d_θ and δ
Return : d_θ , π_ψ , $\{z_k\}_{k=1}^{K}$

4.2 Geometric Foundation : Quasimetric Learning

To enable graph construction and policy learning, we need a calibrated quasimetric function $d_\theta(s, g)$ that estimates the minimum steps to reach g from s. To model such a class of functions, we implement **Interval Quasimetric Embeddings (IQE)** (Wang & Isola, 2022), within the **Quasimetric RL (QRL)** distance function learning framework (Wang et al., 2023).

IQE sets the distance as the aggregated length of intervals in a learned latent space. Given an encoder function $f_{\theta'} : \mathcal{S} \to \mathbb{R}^{N \times M}$, the distance from $x \in \mathcal{S}$ to $y \in \mathcal{S}$ is formed by components that capture the total Lebesgue measure of unions of several intervals on the real line :

$$d_{\theta'}^{(i)}(x, y) = \left| \bigcup_{j=1}^{M} \left[f_{\theta'}(x)_{ij}, \max\left(f_{\theta'}(x)_{ij}, f_{\theta'}(y)_{ij}\right) \right] \right| \tag{1}$$

Using the *maxmean* reduction (Pitis et al., 2020), we obtain IQE-*maxmean* with a single extra trainable parameter $\alpha \in [0, 1]$. Considering $\theta = [\theta', \alpha]$ and $\beta = 1 - \alpha$ we get :

$$d_\theta(x, y) = \alpha \cdot \max\left(d_{\theta'}^{(i)}(x, y)\right) + \beta \cdot \text{mean}\left(d_{\theta'}^{(i)}(x, y)\right) \tag{2}$$

Theorem 4.1. ***IQE General and Universal Approximation*** *(See Wang & Isola 2022) Consider any quasimetric space* $(\mathcal{X}, d)$ *where* $\mathcal{X}$ *is compact and* d *is continuous.* $\forall \epsilon > 0$, $\exists N$, *there exist parameters* $\theta = [\theta', \alpha]$ *such that :* $\forall x, y \in \mathcal{X}$, $\left| d_\theta(x, y) - d(x, y) \right| \leq \epsilon$.

By design, IQE satisfies all the quasimetric properties (Wilson, 1931), while QRL calibrates it by enforcing *local consistency* ($\mathcal{L}_{close}$) and *global separation* ($\mathcal{L}_{push}$) :

$$\mathcal{L}_{close}(\theta) = \mathbb{E}_{(s,s')\sim\mathcal{D}}\left[\lambda \cdot \left(\texttt{relu}(d_\theta(s, s') - 1)^2 - \epsilon^2\right)\right] \tag{3}$$

$$\mathcal{L}_{push}(\theta) = -\,\mathbb{E}_{(s,g)\sim\mathcal{D}}\left[\omega\big(d_\theta(s, g)\big)\right] \tag{4}$$

where ϵ relaxes the local constraint and ω is a monotonically increasing convex function.

Theorem 4.2. ***QRL Value Function Approximation*** *(See Wang et al. 2023) Consider a compact state space $\mathcal{S}$ and an optimal undiscounted value function V^*. Supposing that the state space equals the goal space, if $\{d_\theta\}_{\theta\in\Theta}$ are universal approximators of quasimetric functions over $\mathcal{S}$, then* $\forall\epsilon>0,\ \exists\theta^*\in\Theta, \forall s,g\in\mathcal{S}: \mathbb{P}\Big[\ \big|d_{\theta^*}(s,g)+(1+\epsilon)V^*(s,g)\big|\le\sqrt{\epsilon}\ \Big] = 1-\mathcal{O}\big(-\sqrt{\epsilon}\cdot\mathbb{E}[V^*]\big)$*, i.e. the optimal distance function recovers $-V^*$ up to a scale, with probability of* $1-\mathcal{O}\big(-\sqrt{\epsilon}\cdot\mathbb{E}[V^*]\big)$.

4.3 Topological Abstraction : Keypoints Selection & Planning

Iterative Wavefront Expansion (IWE). We propose IWE as a greedy heuristic to the maximal δ-separated set problem. Defining $d_{\text{sym}}(x,y) := \max(d_\theta(x,y), d_\theta(y,x))$, we add the **closest** candidate $s\in\mathcal{D}$ to the set $\mathcal{Z}$ that satisfies $d_{\text{sym}}(s,z)\ge\delta, \forall z\in\mathcal{Z}$ to enforcing **separation** and **connectivity**.

Algorithm 2 AQM Iterative Wavefront Expansion

Require: *Candidates* $S=\mathcal{D}$; *Quasimetric* d_θ ; *Repel radius* δ
Init: $z_0\sim S$; $\mathcal{Z}\leftarrow\{z_0\}$; $S\leftarrow\{\ s\in S\ \big|\ d_{\text{sym}}(s,z_0)\ge\delta\ \}$
1: **while** $|S|>0$ **do**
2: $\quad z_{\text{new}}\leftarrow\arg\min_{s\in S}\big(\min_{z\in\mathcal{Z}}\ d_{\text{sym}}(s,z)\big)$
3: $\quad\mathcal{Z}\leftarrow\mathcal{Z}\cup\{z_{\text{new}}\}\ ;\ S\leftarrow\{\ s\in S\ \big|\ d_{\text{sym}}(s,z_{\text{new}})\ge\delta\ \}$
4: **end while**
5: **Return** $\mathcal{Z}$.

This greedy strategy, detailed in *Algorithm 2*, grows the graph outwards like a wavefront, so that the keypoints added are reachable from the existing structure, preventing gaps while enforcing a near-uniform sparsity controlled by $\delta>0$. See *Section 5.2.2* for a brief study on the influence of δ.

Dataset Covering. Assuming convergence to the optimal quasimetric function d^*, and defining $d^*_{\text{sym}}(x,y) := \max(d^*(x,y), d^*(y,x))$, *Algorithm 2* returns a δ-cover of the dataset under d^*_{sym} .

Proposition 4.3. ***Covering.*** *Let $\mathcal{M}$ be a compact, path-connected subset of the state space. Assuming $\mathcal{D}$ is ϵ-dense in $\mathcal{M}$ (i.e., $\forall x\in\mathcal{M}, \exists s\in\mathcal{D},\ d^*_{sym}(x,s)<\epsilon$), the set of keypoints $\mathcal{Z}$ generated by Algorithm 2 is a $(\delta+\epsilon)$-cover of $\mathcal{M}$: $\forall x\in\mathcal{M},\ \min_{z\in\mathcal{Z}}\ d^*_{sym}(x,z)<\delta+\epsilon$.*

AQM assumes sufficient coverage of the relevant support. This is often realistic in telemetry-rich settings (e.g., video games), but may be limiting in data-scarce applications. See *Appendices 7* and *8* for more discussions and illustrations.

Graph Construction. From the set of keypoints selected, $\mathcal{Z}=\{z_1,\dots,z_K\}$, we build a *directed* $G=(\mathcal{Z},\mathcal{E})$. Given a radius $\tau>0$, we connect $z_i,z_j\in\mathcal{Z}$ whenever $d^*_{\text{sym}}(z_i,z_j)<\tau$, and add *both* directed edges $(i\to j)$ and $(j\to i)$, with their respective *time-to-reach* as edge weights.

Proposition 4.4. ***Graph Connectivity.*** *Following the above process, with $\tau=2(\delta+\epsilon)$, the underlying undirected graph is connected (hence $G=(\mathcal{Z},\mathcal{E})$ is strongly connected).*

Finally, planning between s and g relies on inferring the shortest path $\mathcal{P}=(s,z_1,\dots,z_n,g)$ over the topological graph, computed via the Floyd-Warshall algorithm described in *Section 3*.

4.4 Learning a Robust Policy

To navigate between keypoints, we train a goal-conditioned policy $\pi_\psi(a|s,g)$. Instead of training a single controller, we leverage a **Policy Bootstrapping** (Zhou & Kao, 2025). This approach focuses on mastering atomic local behaviours, and repurposing them to reach the next subgoal.

During training we maintain a **target policy** π_{ψ^-} and a **main policy** π_ψ. The target policy π_{ψ^-} is trained via Quasimetric Advantage Weighted Regression (Q-AWR) to master *micro-behaviors*, to reach subgoals w sampled from a near future.

$$\mathcal{L}_{\text{T}}(\psi^-) = -\mathbb{E}\left[\exp\Big(\beta_{\text{T}}\cdot\big(d_\theta(s,w)-d_\theta(s',w)\big)\Big)\cdot\log\pi_{\psi^-}(a|s,w)\right] \tag{5}$$

Here (s,a,s') is a transition. The main policy π_ψ is trained to reach any goals g (such as the keypoints) by distilling the target policy's skills. To ensure the short-term action towards w actually contributes to the long-term goal g, we weigh the distillation loss leveraging Quasimetric Subgoal Advantage Weighted (Q-SAW), derived from AWR :

$$\mathcal{L}_M(\psi) = \mathbb{E}\left[\exp\Big(\beta_{\text{M}}\cdot\big(d_\theta(s,g)-d_\theta(w,g)\big)\Big)\cdot D_{\text{KL}}\big(\pi_\psi(\cdot|s,g)\|\pi_{\psi^-}(\cdot|s,w)\big)\right] \tag{6}$$

Intuitively, if the subgoal w lies on the optimal path to g a high importance weight forces the π_ψ to mimic the micro-behavior that leads to w, thus stitching short trajectories into long-horizon plans.

4.5 Geometric Consistency for Adaptive Planning

A novelty introduced by AQM is to exploit the learned quasimetric to enable principled test-time adaptation. For a neighboring pair (z_i, z_{i+1}), we set $B(z_i, z_{i+1}) := (1 + \kappa) \cdot d_\theta(z_i, z_{i+1})$, as a time-to-reach budget, an upper bound of traversal time, with $\kappa \geq 0$ a fixed control-slack parameter. Inference relies on the shortest path $\mathcal{P} = (s, z_1, \ldots, z_n, g)$ over the learned graph, computed via the Floyd-Warshall algorithm described in *Section 3*. To handle environmental shifts at test-time (such as a blocked path), we monitor the elapsed time as the agent traverses an edge. If it exceeds the predicted time-to-reach budget, the learned agent considers the edge as unreliable, marks it as untraversable $\big(d(z_i, z_{i+1}) = \infty \big)$ in the graph, replan an alternative route, enabling zero-shot replanning.

5 Experiments

To empirically validate AQM, we conduct a comprehensive evaluation across a diverse suite of goal-conditioned tasks. Our experiments span standard benchmarks from OGBench (Park et al., 2025a) as well as environments designed to test zero-shot replanning capabilities from Continual NavBench (Kobanda et al., 2025a). We assess performance against flat, hierarchical and graph-based Offline RL methods. Reported results represent the average success rates across multiple seeds. Implementation details and configurations are provided in *Appendices 8*, *9*, and *10*.

5.1 Main Results : How well does AQM perform ?

5.1.1 How effective is AQM on navigation tasks ?

Table 1: **Evaluating Performance (%) on Navigation Tasks from Offline Data.** Baseline results are reported from Baek et al. (2025). Results are averaged over 4 seeds (50 rollouts per goal). Bold values indicate performance with 95% reach of the top performing method.

Dataset Type	AntMaze Dataset	GCBC	GCIQL	QRL	CRL	HILP	HIQL	SAW	GAS	AQM
Locomotion	medium-navigate	33 ± 6	75 ± 5	82 ± 8	**95 ± 1**	**96 ± 1**	**95 ± 1**	**97 ± 1**	**96 ± 1**	**98 ± 1**
	large-navigate	24 ± 3	33 ± 5	75 ± 4	86 ± 5	87 ± 4	**90 ± 2**	**90 ± 2**	**93 ± 1**	**94 ± 2**
	giant-navigate	0 ± 0	0 ± 0	14 ± 4	15 ± 6	53 ± 3	67 ± 6	70 ± 4	78 ± 3	**88 ± 2**
Stitching	medium-stitch	43 ± 8	27 ± 7	67 ± 11	57 ± 8	**96 ± 1**	92 ± 3	**95 ± 2**	**98 ± 1**	**98 ± 2**
	large-stitch	2 ± 4	10 ± 3	20 ± 2	14 ± 6	34 ± 3	72 ± 5	64 ± 9	**97 ± 1**	**95 ± 2**
	giant-stitch	0 ± 0	0 ± 0	0 ± 0	0 ± 0	0 ± 0	1 ± 1	1 ± 2	**88 ± 4**	**90 ± 3**
Exploratory	medium-explore	3 ± 3	12 ± 1	1 ± 1	1 ± 2	40 ± 7	32 ± 3	27 ± 7	**98 ± 0**	**99 ± 1**
	large-explore	0 ± 0	1 ± 1	0 ± 1	0 ± 0	2 ± 2	3 ± 4	5 ± 4	**94 ± 3**	**94 ± 5**

As shown in *Table 1*, our proposed framework **achieves state-of-the-art performance**, consistently outperforming or equaling flat, hierarchical, and graph-based baselines on all environments.

Most flat methods perform reasonably well on `medium` tasks but suffer a collapse in performance on `large` or `giant` tasks, notably when using `stitching` datasets. While hierarchical methods like HIQL and the SAW distillation-based method provide improvements by reasoning, they still exhibit a degradation as the temporal horizon increases. For instance, in `giant-navigate`, they fall behind both AQM and GAS, suggesting that even hierarchical methods struggle with longer horizon tasks.

The results indicate that graph-based frameworks are the only class of navigation algorithms capable of maintaining high success rates in longer horizon settings (above 78 % on `giant` tasks). By modeling the topology of the environments, these methods effectively *stitch* together sparse trajectories, while achieving better performances than hierarchical methods. Beyond this structural advantage, AQM sets a new ceiling for the benchmark, achieving 88 % and 90 % on the most difficult navigation.

5.1.2 Does AQM solve the GAS scaling bottleneck ?

The comparative results displayed in *Table 2* highlight a critical distinction between AQM and GAS. While both are graph-based, **GAS exhibits a heavy reliance on graph density to maintain performance**, whereas **AQM remains highly effective with orders of magnitude fewer nodes**.

This disparity in keypoint count is a decisive barrier for practical deployment. Algorithmic complexity for path-finding methods, such as Floyd-Warshall, scale polynomially with the count ($O(|\mathcal{Z}|^3)$). Moreover, assigning the current state to the nearest keypoint requires querying all keypoints. Thus, as the horizon gets larger, graphs with dense keypoint coverage scales poorly.

In resource-constrained applications, deploying a method that requires 15000 keypoints (as seen with GAS on `antmaze-large-explore`) is a prohibitive burden. By achieving state-of-the-art results with a *leaner* graph, AQM ensures that the topological reasoning is computationally feasible.

Table 2: **Comparison of AQM and GAS Methods.**

AntMaze Dataset	Method	# Nodes	Success (%)
giant-navigate	GAS	4286	74 ± 3
	GAS	978	77 ± 3
	GAS	431	71 ± 2
	GAS	268	64 ± 2
	AQM	**158**	**88 ± 2**
	AQM	**109**	**86 ± 2**
	AQM	**67**	**83 ± 1**
giant-stitch	GAS	12901	81 ± 3
	GAS	1966	88 ± 4
	GAS	688	80 ± 4
	GAS	375	69 ± 2
	AQM	**163**	**90 ± 3**
	AQM	**113**	**88 ± 3**
	AQM	71	82 ± 1
large-explore	GAS	15143	98 ± 1
	GAS	2499	94 ± 3
	GAS	1126	88 ± 8
	GAS	679	90 ± 4
	AQM	**177**	**91 ± 7**
	AQM	**114**	**94 ± 5**
	AQM	**68**	**88 ± 6**

Table 3: **Study of Keypoint Selection Strategies.**

AntMaze Dataset	Selection Strategy	# Nodes	Success (%)
medium-navigate	RND	25	98 ± 1
	RND	**50**	**96 ± 1**
	RND	100	96 ± 2
	FPS	116	97 ± 1
	IWE	**47**	**98 ± 1**
large-navigate	RND	25	78 ± 7
	RND	50	90 ± 6
	RND	100	94 ± 2
	FPS	150	93 ± 3
	IWE	**71**	**94 ± 2**
giant-navigate	RND	25	50 ± 10
	RND	50	54 ± 7
	RND	100	60 ± 5
	FPS	200	72 ± 10
	IWE	**158**	**88 ± 2**

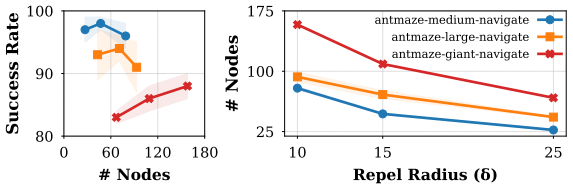

Figure 2: **Performance trade-offs given** δ.

5.1.3 TO WHAT EXTENT DOES OUR APPROACH HANDLE TEST-TIME ADAPTATION ?

We evaluate test-time adaptation on Continual NavBench, where mazes vary with gates (**O** : Open, **X** : Closed) and obstacles (**H** : high or *non-jumpable* / **L** : low or *jumpable*). We compare a subset of representative baselines : **GCBC** (default), **SAW** (best-performing flat policy), **HIQL** (state-of-the-art hierarchical method), and **AQM** (best graph-based method : with high-performance and low cost).

In *Figure 3*, the diagonal results represent evaluations where training and testing environments match. The best results are achieved by AQM (avg. 98), followed by SAW (avg. 88), while HIQL (avg. 80) lags further behind likely due to compounding errors between high-level subgoal generation and low-level execution. GCBC (avg. 53) is struggling on all maps, possibly due to long-horizon and mode averaging. These differences are even more pronounced on the L-maps.

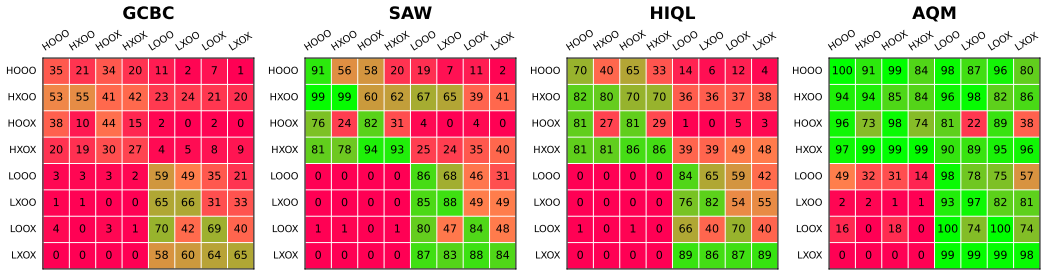

Figure 3: **Evaluating Test-time Adaptation.** Performances are presented as heatmaps where rows represent the training environment and columns represent the evaluation environment. The diagonal values represent standard evaluation setup (training and evaluation environments match), while off-diagonal entries quantify test-time replanning capabilities under specific environmental shifts.

The other results highlight the adaptation capabilities. Within the same obstacles category, AQM demonstrates robust replanning : as a previously open gate is closed ($O \rightarrow X$), the agent must find an alternative path to reach a goal. AQM successfully adapts, using the edge reliability detection and rerouting with the pruned graph. Moreover, agents trained on *non-jumpable* obstacles transfer to *jumpable* ones. This is because the *walk-around* behaviors remain valid, although sub-optimal.

However, transferring from L-maps to H-maps exposes an essential limitation of test-time adaptation : **data support**. In L-map datasets, optimal trajectories involve jumping over obstacles. When deployed in H-maps, these actions are rendered useless, and the learned agents lack the specific *long-detour* skills required. The graph cannot stitch a valid solution from the available transitions. While AQM aims at maximizing the utility of existing knowledge, adaptation remains strictly bounded by the behavioral coverage of the training data. When the necessary recovery skills are absent from the available data, test-time replanning is very difficult.

5.2 Ablation Study : What Makes AQM Work ?

5.2.1 On different keypoints selection strategies

We evaluate Iterative Wavefront Expansion (*Section 4.3*) (IWE) against Random Sampling (RND) and Farthest Point Sampling (FPS). For a fair comparison, FPS and IWE share the same repel radius δ, while RND has various sampling budgets. Resulting mappings are visualized in *Appendix 13*.

As shown in *Table 3*, IWE is efficient. While FPS yields respectable performance, it results in higher node counts, likely since it greedily selects distant points, thus it tends to sample misevaluated outliers due to the QRL *push* loss *(Eq. 4)*. RND tends to fails on larger horizons due to uneven coverage. This confirms that an adapted structured selection process is essential to maintain planning reliability.

5.2.2 On the influence of the repel radius

The repel radius δ (see *Section 4.3*), mitigates the trade-off between efficient mapping and success. As shown in *Figure 2*, increasing δ sharply reduces node counts across all tasks. While success remains stable on `medium` and `large` mazes, in the `giant` one it degrades as the graph thins. This indicates that the graph becomes sparser, success rate is sensitive to the density of subgoals.

5.2.3 On the low policy action control

Table 4: **Study of Low Policy Strategies.**

Dataset	Low Policy	# Nodes	Success
antmaze-giant-navigate	BC	152	21 ± 4
	Q-AWR	152	25 ± 5
	Q-SAW	158	$\mathbf{88} \pm \mathbf{2}$
antmaze-giant-stitch	BC	162	84 ± 7
	Q-AWR	162	83 ± 7
	Q-SAW	163	$\mathbf{90} \pm \mathbf{3}$
antmaze-large-explore	BC	112	0 ± 0
	Q-AWR	112	0 ± 0
	Q-SAW	114	$\mathbf{94} \pm \mathbf{5}$

We study the impact of different l ow-level policy on the performance of AQM. We compare Behavior Cloning (BC), Quasimetric Advantage Weighted Regression (Q-AWR), and Quasimetric Subgoal Advantage Weighted (Q-SAW) which we use by default in AQM. Details on these methods are provided in *Section 4.4*.

As shown in *Table 4*, Q-AWR provides marginal gains over BC but fail on exploratory tasks, while Q-SAW remains efficient. Thus, not leveraging the hierarchical nature of GCRL (Q-AWR) is likely insufficient for long-horizon tasks. Instead, it seems better to leverage hierarchical distillation when using quasimetrics (Q-SAW) to learn useful behaviors.

6 Discussion

We introduced **Adaptive Quasimetric Mapping (AQM)**, a learning framework bridging the gap between geometric representation learning and efficient long-horizon planning. By leveraging covering theory for graph construction, **AQM** approximates a δ-covering of the dataset support. This parsimonious structure enables state-of-the-art performance on navigation benchmarks, computational efficiency, while allowing test-time adaptation. Comprehensive evaluations and analysis show that **AQM** offers a robust and principled solution for deployment in resource-constrained settings.

Nonetheless, adaptive capabilities are bounded by the data support : if specific recovery behaviors are absent, test-time adaptation is difficult. Furthermore, our focus was on deterministic settings. Future work could extend **AQM** to stochastic environments notably via probabilistic graph formulations.

REFERENCES

Eloi Alonso, Maxim Peter, David Goumard, and Joshua Romoff. Deep reinforcement learning for navigation in aaa video games. *Proceedings of the* 30^{th} *International Joint Conference on Artificial Intelligence*, 2020.

Marcin Andrychowicz, Filip Wolski, Alex Ray, Jonas Schneider, Rachel Fong, Peter Welinder, Bob McGrew, Josh Tobin, Abbeel Pieter, and Wojciech Zaremba. Hindsight experience replay. *Advances in neural information processing systems*, 2017.

Kai Arulkumaran, Marc Peter Deisenroth, Miles Brundage, and Anthony Bharath. Deep reinforcement learning : A brief survey. *IEEE Signal Processing Magazine*, 2017.

Seungho Baek, Taegeon Park, Jongchan Park, Seungjun Oh, and Yusung Kim. Graph-assisted stitching for offline hierarchical rl. *International Conference on Machine Learning*, 2025.

Emanuele Balloni, Marco Mameli, Adriano Mancini, and Primo Zingaretti. Deep rl navigation of agents in 2d platform video games. *Computer Graphics International Conference*, 2023.

Christopher Berner, Greg Brockman, Brooke Chan, Vicki Cheung, Przemysław Dębiak, Christy Dennison, David Farhi, Quirin Fischer, Shariq Hashme, and Chris Hesse. Dota 2 with large scale deep reinforcement learning. *Technical Report (Preprint)*, 2019.

James Bradbury, Roy Frostig, Peter Hawkins, Matthew James Johnson, Chris Leary, Dougal Maclaurin, George Necula, Adam Paszke, Jake VanderPlas, Skye Wanderman-Milne, and Qiao Zhang. JAX: Composable transformations of Python+NumPy programs, 2018. URL http://github.com/jax-ml/jax.

Alexi Canesse, Mathieu Petitbois, Ludovic Denoyer, Sylvain Lamprier, and Rémy Portelas. Navigation with qphil : Quantizing planner for hierarchical implicit q-learning. *International Joint Conference on Neural Networks*, 2025.

Oscar Clark. *Games as a service : How free to play design can make better games*. Routledge, 2014.

Xiao Cui and Hao Shi. A*-based pathfinding in modern computer games. *International Journal of Computer Science and Network Security*, 2011.

Vikas Dhiman, Shurjo Banerjee, Jeffrey M Siskind, and Jason J Corso. Learning goal-conditioned value functions with one-step path rewards rather than goal-rewards. *Preprint*, 2018.

Yiming Ding, Carlos Florensa, Mariano Phielipp, and Pieter Abbeel. Goal-conditioned imitation learning. *Advances in Neural Information Processing Systems*, 2019.

Ayoub Echchahed and Pablo Samuel Castro. A survey of state representation learning for deep reinforcement learning. *Transactions on Machine Learning Research*, 2025.

K Anders Ericsson, Ralf T Krampe, and Clemens Tesch-Römer. The role of deliberate practice in the acquisition of expert performance. *Psychological Review*, 1993.

Benjamin Eysenbach, Tianjun Zhang, Sergey Levine, and Russ Salakhutdinov. Contrastive learning as goal-conditioned rl. *Advances in Neural Information Processing Systems*, 2022.

Robert W Floyd. Algorithm 97 : shortest path. *Communications of the Association for Computing Machinery*, 5, 1962.

Michael Fuest, Pingchuan Ma, Ming Gui, Johannes Schusterbauer, Vincent Tao Hu, and Bjorn Ommer. Diffusion models and representation learning: A survey. *IEEE Transactions on Pattern Analysis and Machine Intelligence*, 2024.

Carles Gelada, Saurabh Kumar, Jacob Buckman, Ofir Nachum, and Marc Bellemare. Deepmdp : Learning continuous latent space models for representation learning. *International Conference on Machine Learning*, 2019.

Shangding Gu, Long Yang, Yali Du, Guang Chen, Florian Walter, Jun Wang, and Alois Knoll. A review of safe reinforcement learning: Methods, theories and applications. *IEEE Transactions on Pattern Analysis and Machine Intelligence*, 2024.

Zhiao Huang, Fangchen Liu, and Hao Su. Mapping state space using landmarks for universal goal reaching. *Advances in Neural Information Processing Systems*, 2019.

Leslie Pack Kaelbling. Learning to achieve goals. *International Joint Conference on Artificial Intelligence*, 1993.

Junsu Kim, Younggyo Seo, and Jinwoo Shin. Landmark-guided subgoal generation in hierarchical reinforcement learning. *Advances in neural information processing systems*, 2021.

Anthony Kobanda, CA Valliappan, Joshua Romoff, and Ludovic Denoyer. Learning computational efficient bots with costly features. *IEEE Conference on Games*, 2023.

Anthony Kobanda, Odalric-Ambrym Maillard, and Rémy Portelas. A continual offline reinforcement learning benchmark for navigation tasks. *IEEE Conference on Games*, 2025a.

Anthony Kobanda, Waris Radji, Mathieu Petitbois, Odalric-Ambrym Maillard, and Rémy Portelas. Offline goal-conditioned reinforcement learning with projective quasimetric planning. *European Workshop on Reinforcement Learning*, 2025b.

Ilya Kostrikov, Ashvin Nair, and Sergey Levine. Offline reinforcement learning with implicit q-learning. *International Conference on Learning Representations*, 2022.

Hanna Kurniawati. Partially observable markov decision processes and robotics. *Annual Review of Control, Robotics, and Autonomous Systems*, 2022.

Michael Laskin, Aravind Srinivas, and Pieter Abbeel. Curl: Contrastive unsupervised representations for reinforcement learning. *International conference on machine learning*, 2020.

Sergey Levine, Aviral Kumar, George Tucker, and Justin Fu. Offline reinforcement learning: Tutorial, review, and perspectives on open problems. *Tutorial (Preprint)*, 2020.

Jinning Li, Chen Tang, Masayoshi Tomizuka, and Wei Zhan. Hierarchical planning through goal-conditioned offline reinforcement learning. *IEEE Robotics and Automation Letters*, 2022.

Minghuan Liu, Menghui Zhu, and Weinan Zhang. Goal-conditioned rl : Problems and solutions. *Proceedings of the* 31^{th} *International Joint Conference on Artificial Intelligence*, 2022.

Simon M Lucas, Michael Mateas, Mike Preuss, Pieter Spronck, Julian Togelius, Peter I Cowling, Michael Buro, Michal Bida, Adi Botea, Bruno Bouzy, et al. *Artificial and computational intelligence in games*, volume 6. Citeseer, 2013.

Girolamo Macaluso, Alessandro Sestini, and Andrew D Bagdanov. A benchmark environment for offline reinforcement learning in racing games. *IEEE Conference on Games*, 2024.

Vivek Myers, Bill Chunyuan Zheng, Benjamin Eysenbach, and Sergey Levine. Offline goal-conditioned rl with quasimetric representations. *ArXiv (Preprint) : 2509.20478*, 2025.

Seohong Park, Dibya Ghosh, Benjamin Eysenbach, and Sergey Levine. Hiql: Offline gcrl with latent states as actions. *Advances in Neural Information Processing Systems*, 2023.

Seohong Park, Kevin Frans, Sergey Levine, and Aviral Kumar. Is value learning really the main bottleneck in offline rl ? *Advances in Neural Information Processing Systems*, 2024a.

Seohong Park, Tobias Kreiman, and Sergey Levine. Foundation policies with hilbert representations. *International Conference on Machine Learning*, 2024b.

Seohong Park, Kevin Frans, Benjamin Eysenbach, and Sergey Levine. Ogbench : Benchmarking offline goal-conditioned rl. *International Conference on Learning Representations*, 2025a.

Seohong Park, Kevin Frans, Deepinder Mann, Benjamin Eysenbach, Aviral Kumar, and Sergey Levine. Horizon reduction makes rl scalable. *Advances in Neural Information Processing Systems*, 2025b.

Seohong Park, Aditya Oberai, Pranav Atreya, and Sergey Levine. Transitive reinforcement learning : Value learning via divide and conquer. *ArXiv (Preprint) : 2510.22512*, 2025c.

Xue Bin Peng, Aviral Kumar, Grace Zhang, and Sergey Levine. Advantage-weighted regression : Simple and scalable off-policy rl. *ArXiv (Preprint) : 1910.00177*, 2019.

Silviu Pitis, Harris Chan, Kiarash Jamali, and Jimmy Ba. An inductive bias for distances : Neural nets that respect the triangle inequality. *International Conference on Learning Representations,*, 2020.

Nikolay Savinov, Alexey Dosovitskiy, and Vladlen Koltun. Semi-parametric topological memory for navigation. *International Conference on Learning Representations,*, 2018.

Kun Shao, Zhentao Tang, Yuanheng Zhu, Nannan Li, and Dongbin Zhao. A survey of deep rl in video games. *MIT Art, Design and Technology School of Computing International Conference*, 2019.

Lucy Xiaoyang Shi, Joseph J Lim, and Youngwoon Lee. Skill-based model-based rl. *Proceedings of Machine Learning Research*, 2023.

Lorenzo Steccanella, Joshua B Evans, Özgür Şimşek, and Anders Jonsson. Learning the minimum action distance. *European Workshop on Reinforcement Learning*, 2025.

Richard S Sutton and Andrew G Barto. *Reinforcement Learning : An Introduction, Second Edition*. MIT Press, 2018.

Tongzhou Wang and Phillip Isola. Improved representation of asymmetrical distances with interval quasimetric embeddings. *NeurIPS Workshop on Symmetry and Geometry in Neural Representations*, 2022.

Tongzhou Wang, Antonio Torralba, Phillip Isola, and Amy Zhang. Optimal goal-reaching rl via quasimetric learning. *International Conference on Machine Learning*, 2023.

Wallace Alvin Wilson. On quasi-metric spaces. *American Journal of Mathematics*, Volume 53, 1931.

Shuyuan Zhang, Zihan Wang, Xiao-Wen Chang, and Doina Precup. Incorporating spatial information into goal-conditioned hierarchical reinforcement learning via graph representations. *Transactions on Machine Learning Research*, 2025.

John Luoyu Zhou and Jonathan C Kao. Flattening hierarchies with policy bootstrapping. *Advances in Neural Information Processing Systems,*, 2025.

Xianwen Zhu. Behavior tree design of intelligent behavior of non-player character (npc) based on unity3d. *Journal of Intelligent & Fuzzy Systems*, 2019.

Georg Zoeller. Game development telemetry in production. In *Game analytics: Maximizing the value of player data*. Springer, 2013.

APPENDICES

This supplementary material complements the main paper with additional results, theoretical details, extended discussion, and implementation specificities. Its purpose is to provide a deeper insight, a practical grounding, and support reproducibility.

List of the **Appendices** :

- ***Appendix 7*** **– Video Games, Reinforcement Learning, and Navigation**
  Provides contextual background on offline reinforcement learning in modern video game environments. It discusses the nature of large-scale gameplay datasets, practical constraints in game production, and motivates the relevance of goal-conditioned navigation and adaptive planning in this domain.

- ***Appendix 8*** **– Experimental Setup and Environment Details**
  Details the environments and datasets used in the experiments, including OGBench AntMaze configurations and Continual NavBench. This appendix complements *Section 5* by clarifying environment choices and task variations.

- ***Appendix 9*** **– Baselines**
  Presents the baseline algorithms we used for comparison in our experiments, introduced in *Section 5*, categorizing them into flat (**GCBC**, **GCIQL**, **CRL**, **QRL**, **SAW**), hierarchical (**HIQL**), and graph-based (**HILP**, **GAS**) approaches.

- ***Appendix 10*** **– Implementation Details**
  Provides the implementation details, including network architectures and hyperparameters.

- ***Appendix 11*** **– Proofs**
  Contains the demonstrations for the theoretical claims made in *Section 4.2* and *Section 4.3*

- ***Appendix 12*** **– Additional Results**
  Presents additional quantitative results regarding **AQM**, extending the analysis in *Section 5*.

- ***Appendix 13*** **– Learned State-Space Mappings**
  Offers a qualitative analysis of the topological graphs learned by our approach. Through visualizations of the generated keypoints on different layouts, it illustrates the impact of the repel radius δ and on the resulting graph structure.

7 Video Games, Reinforcement Learning, and Navigation

7.1 Virtual Worlds, Players, and Data

Modern video games are persistent, high-fidelity simulations that track every interactive entity in real time, from character coordinates to environmental triggers (Lucas et al., 2013; Zoeller, 2013). Worldwide platforms routinely generate petabytes of play-logs per month through automatic telemetry pipelines. These logs, often archived for analytics, form unusually clean, richly annotated datasets that are orders of magnitude larger than typical robotics corpora, making video games the ideal frontier for Offline Reinforcement Learning (RL) (Levine et al., 2020; Macaluso et al., 2024).

However developing video games comes with various production constraints: state spaces are often partially observable (Kurniawati, 2022), and both computational and commercial budgets require hard guarantees on players good experience and safety (Kobanda et al., 2023; Gu et al., 2024). Thus, learning frameworks not only have to be data-efficient but also controllable and adaptable to the frequent content updates that characterize the *Games as a Service* model (Clark, 2014).

7.2 From Scripted NPCs to Adaptive Agents

Traditional Non-Player Characters (NPCs) rely on finite-state machines or hand-authored behavior trees (Zhu, 2019). While robust, these scripts are brittle: a slight change in map geometry or a new game mechanic often requires manual re-scripting. While Deep Reinforcement Learning agents have mastered complex video games (Shao et al., 2019), with titles like *Dota 2* (Berner et al., 2019) through massive self-play, the computational cost of such training is prohibitive for most studios.

Consequently, interest has shifted toward *offline* or *offline-to-online* methods that can learn from existing player replays. Our proposed framework, **AQM**, bridges the gap between the robustness of classical *nav-meshes* (Cui & Shi, 2011) and the flexibility of Deep Reinforcement Learning by modeling an environment topology directly from pre-collected player traces.

7.3 Practical Challenges in Game Environments

GCRL is a natural fit for modern games (Alonso et al., 2020; Balloni et al., 2023), in particular Offline GCRL : every quest, checkpoint, or capture flag supplies an explicit goal signal, while replay archives furnish millions of feasible, human-level trajectories on which to train models.

Nevertheless, three practical challenges still limit adoption :

Coverage & Directionality : Replay buffers often sample only a thin manifold of the reachable world. Furthermore, game mechanics are often one-way (e.g., ledge drops, teleporters). AQM addresses this by leveraging a quasimetric distance that respects the inherent asymmetry of these transitions.

Stochasticity : Human behavior and random event triggers (e.g., loot drops or portal destinations) break the deterministic assumptions of standard planners ; consequently policies must be robust to such distributional change, which is not guaranteed by most frameworks. This is a current limitation of AQM and most methods it is tested against.

Environmental Shifts: This is the most critical hurdle. If a developer moves a wall or adds a platform, most offline policies are rendered useless. AQM solves this by considering the learned graph as a dynamic object that can be updated at test-time.

7.4 Adaptive Planning and Environment Design

AQM (see *Section 4*) operationalizes the concept of a *data-driven nav-mesh* designed for zero-shot adaptation. By monitoring a *time-to-reach budget* between topological keypoints, the agent detects obstructions and instantly reroutes through the graph. This mimics human spatial reasoning, where a player finding a blocked path intuitively bypasses it using an internal map of the world.

However, the effectiveness of this replanning is fundamentally a function of dataset coverage. The agent can only reroute if the offline data contains the alternative behaviors required for the new path it must follows. While the massive telemetry available to game companies usually ensures sufficient behavioral coverage, classical benchmarks often lack the specific diversity, such as localized backtracking, needed for recovery in tight corridors. In such *out-of-distribution* cases where a feasible path simply does not exist in the prior data, replanning remains impossible and requiring retraining.

8 Environment Details

8.1 Agents and Mazes

8.1.1 OGBench

OGBench Park et al. (2025a) is a standardized suite of offline goal-conditioned learning tasks. It includes AntMaze, a navigation environment in which a ant-like agent must reach arbitrary goals within bounded mazes of various horizon length.

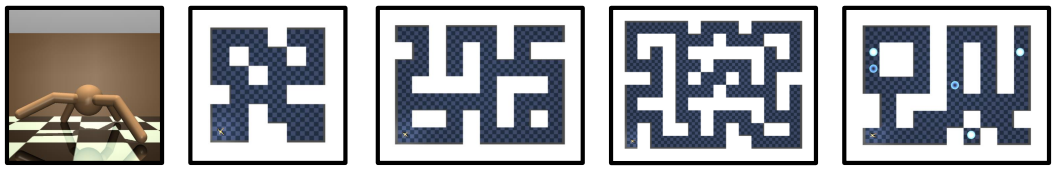

(a) Ant Agent (b) Medium (c) Large (d) Giant (e) Teleport

Figure 4: **OGBench :** AntMaze Agent & Configurations.

Four maze variants appear in OGBench (see *Figure 4*) : `medium` with short trajectory lengths testing basic navigation ; `large` with a longer horizon, increasing the decision complexity ; `giant` scales the maze again, yielding an even larger layout. Although we focused on deterministic environment, we mention the `teleport` configuration which has the same size as the `large` with stochastic portals that randomly chose exits (potentially dead ends).

8.1.2 Continual NavBench

While AntMaze environment allows to efficiently assess navigation performance, it lacks features needed to fully understand how topographic variations affect an agent. Therefore we leverage a video-game like 3D navigation benchmark, namely **Continual NavBench** Kobanda et al. (2025a), that offer diverse mazes with more explainable spatial challenges.

We use the **AmazeVille** suite, with 60 $m \times 60$ m mazes. They have a finite set of start and goal positions, with two subsets of maps : some with high blocks (H), *i.e.* not jumpable obstacles ; others with low blocks (L), *i.e.* jumpable ones.

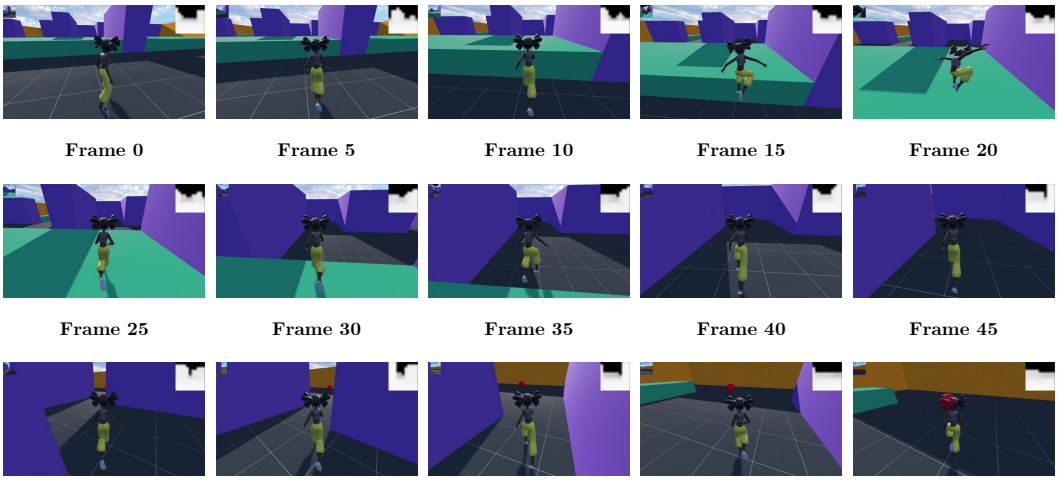

Frame 0 Frame 5 Frame 10 Frame 15 Frame 20

Frame 25 Frame 30 Frame 35 Frame 40 Frame 45

Frame 50 Frame 55 Frame 60 Frame 65 Frame 70

Figure 5: **Continual NavBench :** Visualization of a Human Playing on A-LOOO.

Figure 5 shows a trajectory generated by a human player on one of the maze **A-LOOO**. The naming indicate we are using whether specific doors are open (**O**) or not (**X**), and if movable green blocks are in high positions (**H**) or low positions (**L**), providing a clear way to distinguish between different maze configurations. *Figure 6* displays the different configurations.

Although the maximum number of features an observation may have is 12440, we use (x, y, z) coordinates as the goal space (which provided by default) and the current position, the agent orientation (angle in radian according to the vertical axis), its velocity (in meters per second), and the depth image (as 11×11 raycasts) from its position to the visible nearest obstacles.

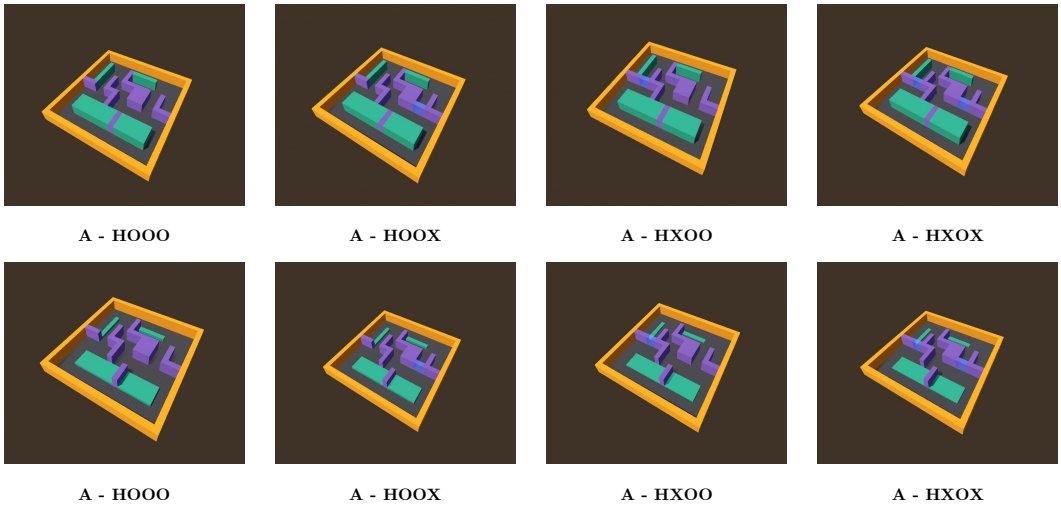

Figure 6: **Continual NavBench :** AmazeVille Maze Configurations.

8.2 Datasets

8.2.1 OGBench

Each AntMaze configurations provide multiple offline datasets : `navigate` contains expert rollouts (1000000 transitions) where a noisy expert wanders toward different goals ; `stitch` breaks those trajectories into shorter ones (200 steps each), forcing to *stitch* discontiguous trajectories ; `explore` consists of random exploratory trajectories (5000000 transitions), designed to test whether the agent can learn navigation skills from extremely low-quality (yet high-coverage)

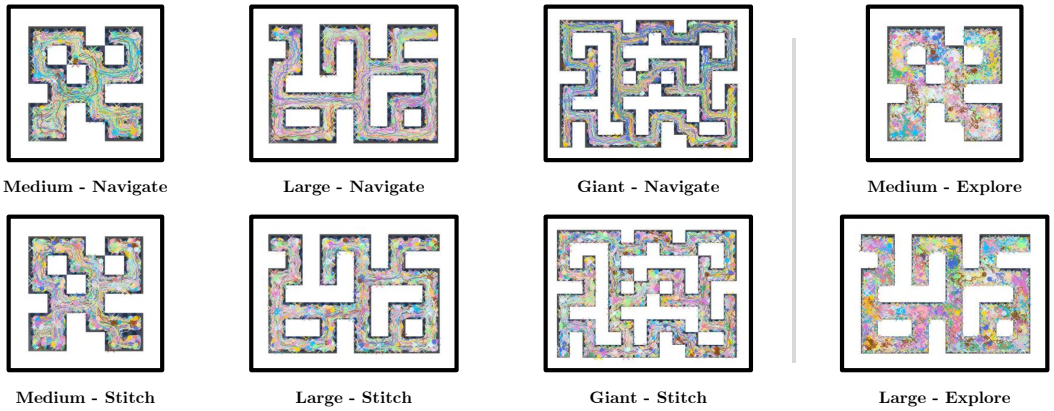

Figure 7: **OGBench :** AntMaze Trajectories Visualization.

Figure 7 displays all available trajectories for the different dataset types. We notably see how densely the trajectories cover each maze configuration for `navigate`, `stitch`, and even more the `explore` datasets. Although we don't investigate the subject, as it is not the main focus of our research, we hypothesis that `explore` datasets are more informative to efficiently learn a distance with QRL Wang et al. (2023), as they provide a broader covering of the set of possible transitions.

8.2.2 Continual NavBench

AmazeVille datasets are all human generated, through hours of play sessions, with 100 episodes for each maze configuration. Consequently, these datasets capture strategies that are potentially valuable for training bots to exhibit human-like behavior.

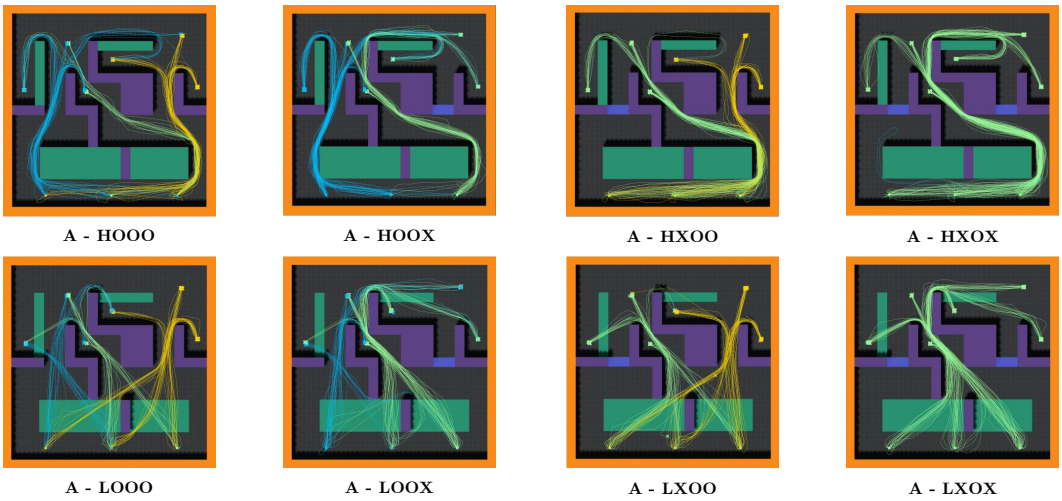

Figure 8: **Continual NavBench :** AmazeVille Trajectories Visualization.

9 BASELINES

This section details the baseline methods used to evaluate AQM. We categorize these into three architectural paradigms Liu et al. (2022) : **flat methods**, which map state-goal pairs directly to actions ; **hierarchical methods**, which decompose tasks using latent subgoals; and **graph-based methods**, which learn and levergae topological structures for navigation.

9.1 FLAT METHODS

Goal-Conditioned Behavioral Cloning (GCBC) (Ding et al., 2019) is the simplest baseline. It treats the problem as a supervised learning task, where a policy is trained to map state-goal pairs directly to the actions found in the dataset. While robust and easy to implement, **GCBC** is inherently limited by the quality of the behavioral data : it cannot *stitch* trajectories or improve upon the suboptimal demonstrations. **AQM** differs by employing an RL-based distance function that allows the agent to reason about reachability and optimality beyond simple imitation.

Goal-Conditioned Implicit Q-Learning (GCIQL) (Kostrikov et al., 2022; Park et al., 2025a) extends Implicit Q-Learning to the goal-conditioned setting. It avoids the overestimation issue common in offline RL by using expectile regression to estimate the value of the best action within the dataset's support without ever querying out-of-distribution actions. While **GCIQL** is a strong baseline for medium-horizon tasks, it struggles with the compounding value-estimation errors of long-horizon navigation. **AQM** addresses this by decomposing the problem into a sequence of local, graph-guided sub-tasks.

Contrastive Reinforcement Learning (CRL) (Eysenbach et al., 2022) leverages contrastive learning to represent the value function. It trains a critic to distinguish between states that are near each other in time and states that are far, effectively learning a representation where the dot product of state-goal embeddings correlates with reachability. However, **CRL** distances are often uncalibrated and represent relative similarities rather than true temporal distances. **AQM** improves upon this by using a quasimetric formulation specifically calibrated to estimate time-to-reach values.

Quasimetric Reinforcement Learning (QRL) (Wang et al., 2023) is a principled approach that learn quasimetric. It enforces the triangle inequality as a structural prior during training, allowing for robust distance estimation. While **AQM** adopts a similar quasimetric learning framework, we expand it by integrating a parsimonious keypoint selection strategy and a graph-based planning layer, moving from a pure distance-learning method to an explicit space mapping and goal-reaching system that reduces reliance on long-horizon value or trajectory prediction.

Subgoal Advantage-Weighted Policy Bootstrapping (SAW) (Zhou & Kao, 2025) is a flat offline GCRL method that targets long-horizon control without hierarchical inference. It trains a single goal-conditioned policy by sampling intermediate *subgoals* from dataset trajectories and regressing the policy toward the actions that reach these subgoals, with updates *advantage-weighted* so that subgoals inducing stronger progress toward the final goal dominate learning. This provides a simple, effective form of stitching while staying within dataset support. **AQM** leverages a related subgoal decomposition intuition, but uses a learned time-to-reach quasimetric as the core decision signal, deriving advantages and graph edges from it to better control long-horizon composition.

9.2 Hierarchical Methods

Hierarchical methods leverage a multi-level structure where a high-level policy selects intermediate subgoals for a low-level controller to achieve. To represent this paradigm, we compare against the current state-of-the-art.

Hierarchical Implicit Q-Learning (HIQL) (Park et al., 2023) is the SOTA representative for Hierarchical GCRL. it uses a high-level policy to pick latent subgoals from the dataset, which a low-level policy then pursues. This hierarchy allows the agent to reason across longer temporal horizons than flat methods. However, **HIQL**'s reliance on latent spaces can make performance sensitive to representation quality and subgoal selection errors over long horizons. **AQM** instead plans over an explicit sparse keypoint graph constructed from calibrated time-to-reach estimates, which provides a simple, interpretable abstraction for long-horizon composition.

9.3 Graph-Based Methods

Graph-based methods explicitly build a topological map of the environment, where nodes represent states and edges represent feasible transitions. We compare our approach against most ones.

Hilbert Foundation Policies (HILP) (Park et al., 2024b) learn a geometric state embedding ϕ into a Hilbert space where Euclidean distances $\|\phi(s) - \phi(g)\|$ approximate long-horizon temporal distances, and train a latent-conditioned policy to follow *directions* in this learned geometry. Goal-reaching can then be performed by choosing directions consistent with the embedding, using ϕ as an implicit topological abstraction. However, HILP's success hinges on the accuracy of the learned geometry, and the method does not directly control graph sparsity or planning complexity. **AQM** instead builds an explicit sparse graph, where edge weights are grounded in a learned time-to-reach quasimetric, enabling efficient planning while reducing reliance on long-horizon trajectory prediction.

Graph-Assisted Stitching (GAS) (Baek et al., 2025) is the SOTA representative for graph-based navigation. It builds a graph by clustering the dataset and creating edges based on temporal proximity. While **GAS** is highly effective at solving complex mazes, it reflects a broader trend in the field where SOTA performance is increasingly attainable, yet few methods remain geometrically principled or computationally parsimonious. **GAS** typically requires a high density of nodes and substantial planning overhead as problem scale increases. **AQM** distinguishes itself by using a mathematically grounded dominating-set-inspired selection strategy to build substantially sparser graphs, and by leveraging time-to-reach calibration to gate edges, which improves computational efficiency.

10 Implementation Details

We use **JAX** Bradbury et al. (2018) as our learning framework. Unless otherwise stated, we follow the experimental protocol from **OGBench** Park et al. (2025a) and keep all unspecified hyperparameters identical ; the deviations are reported below.

10.1 Network Architectures

Backbones. If not otherwise stated, all networks (quasimetric encoder and policy networks) are MLPs with 3 hidden layers of width 512 and GELU activations. Only for IQE we use LayerNorm in each MLP block (after the nonlinearity).

Interval Quasimetric Embedding (IQE). We parameterize the quasimetric using Interval Quasimetric Embeddings (IQE) (Wang & Isola, 2022) with 512 components of size 1 (i.e., a 512×1 latent reshaping). In the original IQE formulation, a common choice is 64 components of size 8. We found the two parameterizations to yield comparable performance in our setting, but the 512×1 variant is significantly faster in our JAX implementation due to simpler element-wise operations.

Actor Policies. Policies are goal-conditioned and follow the same MLP backbone described above. Unless otherwise stated, we keep parameterizations and initialization identical to **OGBench** defaults.

10.2 Hyperparameters & Optimization

We use the Adam optimizer for all modules. All policy networks are trained with learning rate $\eta_\pi = 3 \times 10^{-4}$ and batch size $B = 1024$. The IQE quasimetric encoder is trained with learning rate $\eta_d = 1 \times 10^{-4}$, the Quasimetric RL Lagrange multiplier is initialized at $\lambda = 1.0$ and trained with a learning rate $\eta_\lambda = 1 \times 10^{-2}$. For advantage-weighted policy updates (from SAW and HIQL, to Q-AWR and Q-SAW objectives) we set the temperature to $\alpha = 3.0$. All of our experiments run for 10^6 gradient steps. Results are averaged over the same **four seeds** per training environment and dataset.

Training is performed on NVIDIA V100 GPUs. Typical wall-clock time ranges from about 2 hours on **OGBench** to about 4 hours on **Continual NavBench**, largely due to evaluation overhead (simulation runtime) rather than gradient computation.

In QRL (for $\mathcal{L}_{\text{push}}$ in Eq. 4), we use the strictly monotonically increasing convex function, with m as offset and s as scale :

$$\omega(x) \triangleq -\operatorname{softplus}\big(m - x, \beta = s\big) = -\frac{\operatorname{softplus}\big(s \cdot (m - x)\big)}{s}.$$

Table 5: Offset and Scale Hyperparameters per Dataset.

Dataset	**Offset** (m)	**Scale** (s)
antmaze-medium-{navigate, stitch, explore}	50.0	0.01
antmaze-large-{navigate, stitch, explore}	125.0	0.01
antmaze-giant-{navigate, stitch, explore}	250.0	0.01
AmazeVille	100.0	0.01

Keypoint Separation Sweep. We sweep the IWE radius δ and report the best performance for each dataset. For AntMaze we sweep $\delta \in \{10, 15, 25\}$, and for AmazeVille we sweep $\delta \in \{5, 10\}$. For low-level subgoal horizons, we sweep $\{5, 10, 15\}$.

10.3 Data Sampling & Processing

We use **OGBench** Offline datasets described in *Appendix 8*.

Goal and subgoal sampling. In AQM, goals are sampled from future states along the same trajectory, except for `explore` datasets where goals are sampled uniformly at random. Subgoals are sampled at a fixed future offset (see previous section).

Direction-Conditioned Policies (Continual NavBench). On Continual NavBench, we condition both low-level and high-level policies on the *direction* to the (sub)goal, i.e., $\Delta g = \frac{g-s}{\|g-s\|}$, instead of the absolute goal coordinate. We apply this to all goal-conditioned methods with hierarchical interfaces (SAW, HIQL, AQM).

Scope Note (Continual NavBench). Continual NavBench is designed to stress adaptation under distribution shift; its logged trajectories may not provide diverse alternative paths. Since the goal space in this setting lies in $\mathbb{R}^3$, with additional engineering (e.g., injecting stochasticity, memory, or explicit exploration during data collection), policy-only baselines might partially mitigate some failure modes, but would likely lack AQM's test-time graph pruning mechanism and lack behind.

10.4 Discussions

On Evaluation Protocols. For AntMaze baselines, we report the numbers from the GAS Baek et al. (2025) and evaluate our methods under the *same* protocol (dataset versions, evaluation procedure, and reporting). This reuse is standard practice on established benchmarks and allows rapid, controlled comparisons without redundant retraining when protocols are aligned. The only baseline we reran for AntMaze is SAW Zhou & Kao (2025), since it is not reported in the GAS paper; we ran SAW using the official implementation and default settings, matching the same evaluation protocol used for our methods.

On Runtime Comparisons. We do not report cross-paper wall-clock comparisons because implementations span different frameworks, engineering choices, and heterogeneous hardware stacks ; *naïve* timing would mix algorithmic effects with software-level artifacts. A fair runtime study would require a unified, carefully engineered setup, which was out of scope here ; we therefore focus on protocol-matched performance metrics and on the algorithmic analysis presented in the paper.

11 Proofs

We provide the demonstrations for the theoretical claims made in *Section 4.2* and *Section 4.3*. We focus on two properties of the keypoint set produced by **Iterative Wavefront Expansion** :

(i) Covering guarantee (*Proposition 4.3*) ;

(ii) Connectivity of the induced keypoint graph (*Proposition 4.4*) .

11.1 Assumptions and Notation

Let the state space be a subset $\mathcal{X} \subset \mathbb{R}^n$, $\mathcal{D} \subseteq \mathcal{X}$ be a set of states, and let $\mathcal{M} \subseteq \mathcal{X}$ denote its support.

A1. Compactness and Connectivity. We assume $\mathcal{M}$ is compact and a path-connected subset of $\mathcal{X}$.

A2. Optimality. We assume convergence to an optimal time-to-reach quasimetric $d^* : \mathcal{X} \times \mathcal{X} \to \mathbb{R}^+$.

We define the symmetrized distance as : $d^*_{\text{sym}}(x, y) := \max \left\{ d^*(x, y) \, , \, d^*(y, x) \right\}$.

A3. Density. Let $\epsilon > 0$. $\mathcal{D}$ is ϵ-dense in $\mathcal{M}$ w.r.t. d^*_{sym} : $\forall x \in \mathcal{M} \, , \, \exists s \in \mathcal{D}$ s.t. $d^*_{\text{sym}}(x, s) < \epsilon$.

11.2 Preliminary Lemmas

Lemma 11.1 (Symmetrized Metric). *Assuming **A2**, d^*_{sym} is a metric on $\mathcal{X}$.*

Proof. We verify the metric axioms :

Non-negativity : Since $d^*(x, y) \geq 0$ and $d^*(y, x) \geq 0$, $d^*_{\text{sym}}(x, y) = \max\{d^*(x, y), d^*(y, x)\} \geq 0$.

Identity of indiscernibles : If $x = y$, then $d^*(x, y) = d^*(y, x) = 0$, hence $d^*_{\text{sym}}(x, y) = 0$.
Conversely, if $d^*_{\text{sym}}(x, y) = 0$, then $d^*(x, y) = 0$ and $d^*(y, x) = 0$, which implies $x = y$.

Symmetry : By definition : $d^*_{\text{sym}}(y, x) = \max\{d^*(y, x), d^*(x, y)\} = d^*_{\text{sym}}(x, y)$.

Triangle inequality : By the directed triangle inequality for d^* :

$$d^*(x, z) \leq d^*(x, y) + d^*(y, z) \leq d^*_{\text{sym}}(x, y) + d^*_{\text{sym}}(y, z).$$

Applying the same argument to the reversed direction yields :

$$d^*(z, x) \leq d^*(z, y) + d^*(y, x) \leq d^*_{\text{sym}}(y, z) + d^*_{\text{sym}}(x, y) = d^*_{\text{sym}}(x, y) + d^*_{\text{sym}}(y, z).$$

Taking the maximum of the two left-hand sides gives :

$$d^*_{\text{sym}}(x, z) = \max\{d^*(x, z), d^*(z, x)\} \leq d^*_{\text{sym}}(x, y) + d^*_{\text{sym}}(y, z),$$

which proves the triangle inequality, and the lemma. □

Lemma 11.2 (Termination). *Assuming **A2**, Algorithm 2 terminates in a finite amount of iterations.*

Proof. At each iteration, the algorithm selects a keypoint $z \in S$ and updates :

$$S \leftarrow \{ s \in S \mid d^*_{\text{sym}}(s, z) \geq \delta \}.$$

Since $d^*_{\text{sym}}(z, z) = 0 < \delta$, the selected point z is always removed by the pruning step, i.e., $z \notin S$.

While $S \neq \emptyset$ holds, the cardinality strictly decreases : $|S_{k+1}| \leq |S_k| - 1$. Since $\mathcal{D}$ is finite, this cannot occur indefinitely and after at most $|\mathcal{D}|$ iterations, the algorithm terminates with $S = \emptyset$. □

11.3 Dataset covering

Dataset Covering. Assuming **A2**, *Algorithm 2* returns a δ-cover of the dataset under d^*_{sym} .

Proof. *Algorithm 2* initializes $S \leftarrow \mathcal{D}$ and iteratively selects a keypoint $z \in S$, adds it to $\mathcal{Z}$, then removes from S all points s such that $d^*_{\text{sym}}(s, z) < \delta$. The algorithm terminates only when $S = \emptyset$. Therefore every dataset point $s \in \mathcal{D}$ must have been removed at some iteration due to being within d^*_{sym}-distance $< \delta$ of a selected keypoint, i.e.: $\forall s \in \mathcal{D}$, $\exists z \in \mathcal{Z}$ s.t. $d^*_{\text{sym}}(s, z) < \delta$. Hence $\mathcal{Z}$ is a δ-cover of $\mathcal{D}$ under d^*_{sym} . □

11.4 Proof of *Proposition 4.3* (Covering)

Proposition 4.3. *Assuming **A1**, **A2**, and **A3**, the set of keypoints $\mathcal{Z}$ generated by Algorithm 2 is a $(\delta + \epsilon)$-cover of $\mathcal{M}$.*

Proof. Fix any $x \in \mathcal{M}$. By ϵ-density, $\exists\, s \in \mathcal{D}$ such that $d^*_{\text{sym}}(x, s) < \epsilon$.

By the Dataset Covering result above, $\exists\, z \in \mathcal{Z}$ such that $d^*_{\text{sym}}(s, z) < \delta$. Using *Lemma 11.1* :

$$d^*_{\text{sym}}(x, z^\star) \leq d^*_{\text{sym}}(x, s) + d^*_{\text{sym}}(s^\star, z^\star) < \epsilon + \delta.$$

Since x was arbitrary, $\mathcal{Z}$ is a $(\delta + \epsilon)$-cover of $\mathcal{M}$. □

11.5 Graph Construction

Graph Construction. Assuming **A1**, **A2**, and **A3**, with the selected keypoints $\mathcal{Z} = \{z_1, \ldots, z_K\}$ by *Algorithm 2*, we build a directed graph $G = (\mathcal{Z}, \mathcal{E})$. Given a radius $\tau > 0$, we connect $z_i, z_j \in \mathcal{Z}$ whenever $d^*_{\text{sym}}(z_i, z_j) < \tau$, and add *both* directed edges $(i \to j)$ and $(j \to i)$ with weights $d^*(z_i, z_j)$ and $d^*(z_j, z_i)$, respectively.

11.6 Proof of *Proposition 4.4* (Connectivity)

Proposition 4.4. *Assuming **A1**, **A2**, and **A3**, and following the aforementioned construction process, with $\tau = 2(\delta + \epsilon)$, the underlying undirected graph is connected (hence G is strongly connected) .*

Proof. Let $R := \delta + \epsilon$ and $\tau := 2R$.

Assume for contradiction that the underlying undirected graph is disconnected.

Then $\mathcal{Z}$ can be partitioned into two non-empty disjoint sets A and B such that no edge crosses the cut.

By the edge rule, this implies that $\forall\, a \in A, \forall\, b \in B \;:\; d^*_{\text{sym}}(a, b) \geq \tau = 2R$.

We define two open subsets of $\mathcal{M}$ (as unions of open balls) :

$$U_A := \bigcup_{a \in A} \{x \in \mathcal{M} : d^*_{\text{sym}}(x, a) < R\} \quad , \quad U_B := \bigcup_{b \in B} \{x \in \mathcal{M} : d^*_{\text{sym}}(x, b) < R\}.$$

Covering : By Proposition 4.3, $\mathcal{Z} = A \cup B$ is an R-cover of $\mathcal{M}$, hence $\mathcal{M} \subseteq U_A \cup U_B$.

Disjointedness : If $x \in U_A \cap U_B$, then $\exists\, a \in A$, $\exists\, b \in B$ such that $d^*_{\text{sym}}(x, a) < R$, $d^*_{\text{sym}}(x, b) < R$. By *Lemma 11.1*, $d^*_{\text{sym}}(a, b) \leq d^*_{\text{sym}}(a, x) + d^*_{\text{sym}}(x, b) < 2R = \tau$, contradicting $d^*_{\text{sym}}(a, b) \geq \tau$. Hence $U_A \cap U_B = \emptyset$.

Contradiction : We have written $\mathcal{M}$ as a union of two disjoint non-empty open sets, contradicting **A1**.

Therefore the underlying undirected graph must be connected.

Strong connectivity of G : Since for every undirected adjacency we add both directed edges, any undirected path in the underlying graph lifts to a directed path in G. Thus G is strongly connected. □

11.7 Discussion: assumptions vs. practice

The previous results are stated under clean assumptions to make the guarantees explicit.

We now clarify :

(i) Why these assumptions are reasonable in our experimental setting ;

(ii) When they may fail ;

(iii) How the theory connects to the practical implementation .

On A1 (Compactness and Connectivity).

We assume $\mathcal{M} \subseteq \mathcal{X} \subset \mathbb{R}^n$ is compact and path-connected. In the navigation domains considered here, the relevant state variables are either inherently bounded (e.g., positions in a bounded map, bounded joint angles or velocities after clipping, bounded observations by design), or are effectively restricted to a bounded region of interest by the dataset support. This motivates compactness as a modeling assumption.

Path-connectedness is also natural for the *reachable* subset of states induced by a single environment layout : for instance, a continuous workspace (or maze free-space) typically forms one connected component when obstacles do not fully separate the space. In practice, we observe this behavior on our datasets: see *Appendix 8* for qualitative visualizations in OGBench showing that the collected states concentrate on a dense, coherent region.

Failure modes. A1 can be violated when the dataset mixes multiple disconnected supports : data aggregated from distinct maps with no overlap ; multiple rooms separated by closed doors never opened in data ; multi-modal resets that place the agent in disjoint regions with no trajectories connecting them. In such cases, IWE still produces a cover of $\mathcal{D}$, but *Proposition 4.4* may fail because the true support contains multiple connected components ; correspondingly, a single connected planning graph is not the right abstraction. Our method is therefore most appropriate when the dataset covers a single connected region of the task support.

On A2 (Convergence to the Optimal Quasimetric, and a Realistic Extension).

The previous proofs assume convergence of the learned quasimetric to d^* to keep the statements simple. In practice, we only have access to an approximation d_θ. A natural extension is to introduce a uniform approximation error ε_q such that, for all x, y in the relevant support :

$$\left|d_\theta(x, y) - d^\star(x, y)\right| \leq \varepsilon_q \quad , \quad \left|d_{\text{sym},\theta}(x, y) - d^\star_{\text{sym}}(x, y)\right| \leq \varepsilon_q \ ,$$

which would propagate through the inequalities used in *Proposition 4.3* and *Proposition 4.4*. Concretely, covering and connectivity radii would inflate by an additive term on the order of ε_q (e.g., $(\delta + \epsilon)$ becomes $(\delta + \epsilon + \varepsilon_q)$, and τ inflates accordingly), making explicit how approximation error weakens the guarantees.

Quantifying the quality of a learned quasimetric in continuous spaces is difficult: there is no single scalar metric that simultaneously captures triangle inequality tightness, calibration to time-to-reach, and usefulness for planning. In our work, we therefore rely on two practical diagnostics: (i) qualitative inspection of learned mappings (*Appendix 13*), and (ii) downstream behavioural validation.

On A3 (Dataset ϵ-density).

The ϵ-density assumption is a standard way to formalize "coverage" of the relevant support. In telemetry-rich settings (e.g., video games), large-scale logging often produces dense state visitation in the regions of interest. This is consistent with our empirical setting: visualizations in *Appendix 8* suggest that OGBench datasets are sufficiently dense for the covering and connectivity arguments.

Limitation under scarce data. When data are sparse, large holes appear in the support and ϵ becomes large, weakening the theoretical radius $\tau = 2(\delta + \epsilon)$ and, more importantly, degrading planning quality in practice. In that regime, AQM is expected to fail or require additional mechanisms (e.g., exploration, data augmentation, or stronger priors on dynamics) since sparse offline data fundamentally limits long-horizon navigation.

Unknown ϵ and choice of τ (we do not set $\tau = 2(\delta + \epsilon)$).

The parameter ϵ is not directly observable in high-dimensional continuous-control domains. Hence, we do not instantiate the theoretical threshold $\tau = 2(\delta + \epsilon)$. Instead, we use a simple conservative proxy consistent with the IWE intuition:

$$\tau := 2\delta \quad \text{(optionally with a small slack)}.$$

This choice empirically yields well covering and connected graphs across our benchmarks, while avoiding density estimation.

Batch-based Keypoint Selection (JAX-friendly).

For compilation and memory reasons, we run IWE on a large subset $\mathcal{D}_B \subset \mathcal{D}$ rather than the full dataset. The theoretical statements then apply to the sampled support induced by $\mathcal{D}_B$. In practice, we mitigate this by setting $|\mathcal{D}_B|$ to 1024 and repeating IWE over multiple batches, selecting the one with the most keypoints. Empirically, we find that the resulting graphs remain stable once the batch is large enough to reflect the dataset geometry.

(Optional) Connectivity by construction.

A robust implementation-level alternative, independent of ϵ, is to record at insertion time the attachment distance $\rho_{k+1} := \min_{z \in Z_k} d_{\text{sym}}(z_{k+1}, z)$ and explicitly include the corresponding parent edge. This guarantees connectivity for any threshold $\tau \geq \max_k \rho_{k+1}$ and can be used as a safety mechanism, especially when density is hard to assess.

12 ADDITIONAL RESULTS

12.1 NAVIGATION

Table 6: **Sensitivity to subgoal distance (H-Step) and separation radius δ on `antmaze-medium`.** Entries report success rate (%) as mean ± std over seeds.

Dataset Type	AntMaze Task	H-Step	$\delta = 10.0$	$\delta = 15.0$	$\delta = 25.0$
Locomotion	navigate	10	95.6 ± 2.4	97.6 ± 2.3	95.6 ± 1.5
	navigate	15	96.4 ± 2.3	95.4 ± 4.3	97.2 ± 1.3
	navigate	25	95.8 ± 2.3	98.0 ± 1.4	96.8 ± 1.6
Stitching	stitch	10	97.0 ± 1.9	93.8 ± 8.4	96.2 ± 2.2
	stitch	15	96.6 ± 2.3	91.8 ± 9.0	96.2 ± 1.1
	stitch	25	97.6 ± 1.8	96.2 ± 0.8	97.4 ± 1.8
Exploratory	explore	10	99.6 ± 0.5	99.4 ± 0.9	98.6 ± 1.3
	explore	15	99.4 ± 0.9	99.0 ± 0.7	98.6 ± 1.3
	explore	25	99.4 ± 0.9	97.8 ± 1.8	99.0 ± 1.0

Table 7: **Sensitivity to subgoal distance (H-Step) and separation radius δ on `antmaze-large`.** Entries report success rate (%) as mean ± std over seeds.

Dataset Type	AntMaze Task	H-Step	$\delta = 10.0$	$\delta = 15.0$	$\delta = 25.0$
Locomotion	navigate	10	91.8 ± 1.6	92.2 ± 3.6	92.2 ± 2.6
	navigate	15	90.8 ± 3.5	94.0 ± 1.6	93.4 ± 4.1
	navigate	25	92.2 ± 1.6	90.4 ± 4.3	91.2 ± 4.1
Stitching	stitch	10	94.8 ± 1.9	93.8 ± 3.1	87.8 ± 8.0
	stitch	15	92.4 ± 4.0	90.4 ± 3.6	90.6 ± 2.2
	stitch	25	92.8 ± 4.0	92.0 ± 1.0	89.4 ± 10.1
Exploratory	explore	10	90.6 ± 7.3	94.0 ± 4.5	83.2 ± 25.7
	explore	15	86.4 ± 16.4	87.8 ± 5.9	81.0 ± 22.4
	explore	25	86.2 ± 2.8	78.6 ± 22.2	88.2 ± 5.7

Table 8: **Sensitivity to subgoal distance (H-Step) and separation radius δ on `antmaze-giant`.** Entries report success rate (%) as mean ± std over seeds.

Dataset Type	AntMaze Task	H-Step	$\delta = 10.0$	$\delta = 15.0$	$\delta = 25.0$
Locomotion	navigate	10	85.2 ± 7.0	84.0 ± 2.5	80.6 ± 3.2
	navigate	15	87.8 ± 1.5	85.6 ± 1.9	82.8 ± 1.3
	navigate	25	85.0 ± 4.8	85.6 ± 3.4	84.2 ± 2.6
Stitching	stitch	10	86.4 ± 3.8	82.0 ± 2.1	81.0 ± 9.1
	stitch	15	90.4 ± 3.3	88.0 ± 3.1	82.2 ± 1.1
	stitch	25	90.4 ± 4.2	87.6 ± 4.0	80.0 ± 4.8

12.2 REPLANNING

12.2.1 REPLANNING – BENCHMARK

Figure 9) shows the evaluation on a cross-environment generalization task: diagonal entries are in-distribution (training and evaluation environments match), while off-diagonal entries measure test-time adaptation under environment shifts. SAW and HIQL improve over GCBC and generalize to some shifted environments, but still exhibit large off-diagonal drops under harder shifts. In contrast, AQM maintains strong performance not only on the diagonal but also across many off-diagonal entries, indicating effective zero-shot replanning: when transitions become invalid under shifts, AQM can prune and reroute rather than committing to the original plan.

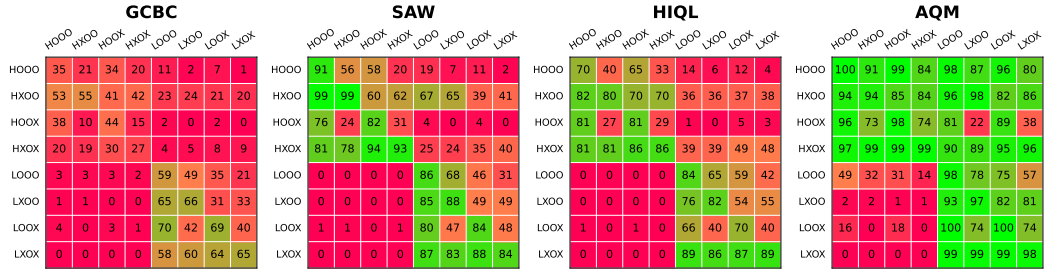

Figure 9: **Evaluating Test-time Adaptation.** Performances are presented as heatmaps where rows represent the training environment and columns represent the evaluation environment. The diagonal values represent standard evaluation setup (training and evaluation environments match), while off-diagonal entries quantify test-time replanning capabilities under specific environmental shifts.

12.2.2 REPLANNING – ABLATION

Figure 10 shows an ablation on two AQM design parameters: (i) the keypoint separation radius δ, which controls how sparse the keypoint set is (smaller δ yields more keypoints) ; (ii) the subgoal sampling distance K, which controls how far ahead subgoals are sampled during training. Increasing K from 5 to 10 generally improves transfer and adaptation (off-diagonal entries), with gains most visible in harder settings (L-maps $\rightarrow$ H-maps), consistent with longer-horizon subgoals improving the ability to bridge between keypoints. Varying δ induces a trade-off between coverage and robustness: smaller δ produces denser graphs that can perform well in-distribution but may be less stable under pruning, whereas larger δ yields sparser abstractions that remain robust provided the graph stays sufficiently connected. Overall, the most uniform performance across shifts (visually the "greenest" off-diagonal pattern) is obtained for the combination $\delta = 10$ and $K = 10$.

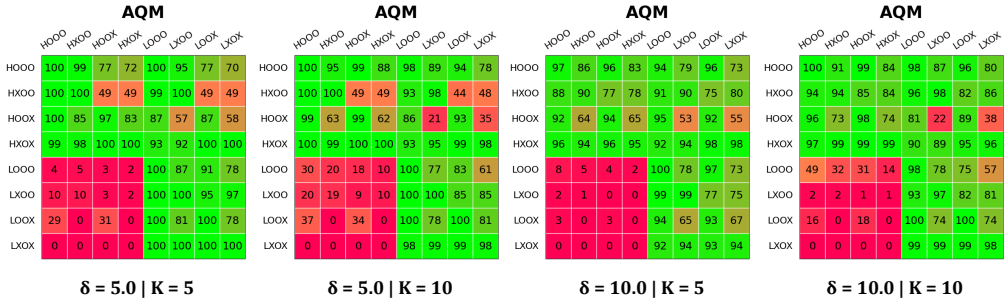

Figure 10: **AQM hyperparameter sensitivity.** Performance heatmaps of AQM as a function of the separation radius δ (controls keypoint sparsity) and the subgoal sampling distance K (controls how far subgoals are sampled along trajectories). Rows denote the training environment and columns denote the evaluation environment.

13 Learned State-Space Mappings

13.1 Analysis of Learned Mappings

Figures 11, *12*, and *13* visualize the topological graphs learned by **AQM** across the `medium`, `large`, and `giant` mazes. Specifically, they depict the spatial distribution of the selected sets of keypoints (red dots) relative to the environment layout.

Influence of the Repel Radius (δ) : As expected, we observe a strict inverse relationship between the repel radius and graph density. At $\delta = 10.0$ the algorithm produces a dense covering that captures granular connectivity and small paths. At $\delta = 25.0$ the graph is significantly pruned, retaining higher level topological representation of the maze. Crucially, regardless of the δ value, the spatial distribution remains uniform across the reachable manifold. The keypoints respect the environment's geometry solely based on the learned quasimetric and available transitions.

Influence of the Dataset : The mappings derived from `navigate` and `stitch` datasets exhibit highly similar densities and distributions. However, mappings generated from the `explore` datasets appear consistently denser, particularly at lower δ values. This can notably be attributed to the nature of the data : the `explore` dataset contains 5 times more transitions (5 M vs 1 M) and consists of random walks that cover the state-action space more exhaustively than the directed, task-oriented trajectories of the other datasets. This increased data density provides the dominating set algorithm with a larger pool of candidates, allowing it to fill minor topological gaps that might be sparsely represented in the expert datasets.

Interestingly enough, these visualizations underscore the potential of the generated graphs as diagnostic tools for exploration in Online RL or data collection in Offline RL. Because the keypoint distribution mirrors the support of the collected data, the topological structure effectively delineates the boundaries of the agent's knowledge. Thus, gaps in the graph may serve as explicit indicators of missing transitions or barriers. Following contemporary research Zhang et al. (2025), this suggests a promising avenue for leveraging this *topological uncertainty* to guide active exploration, where an agent prioritizes data collection in regions where the manifold approximation is fragmented, thereby progressively refining the topological graph.

13.2 OGBench – AntMaze – Medium

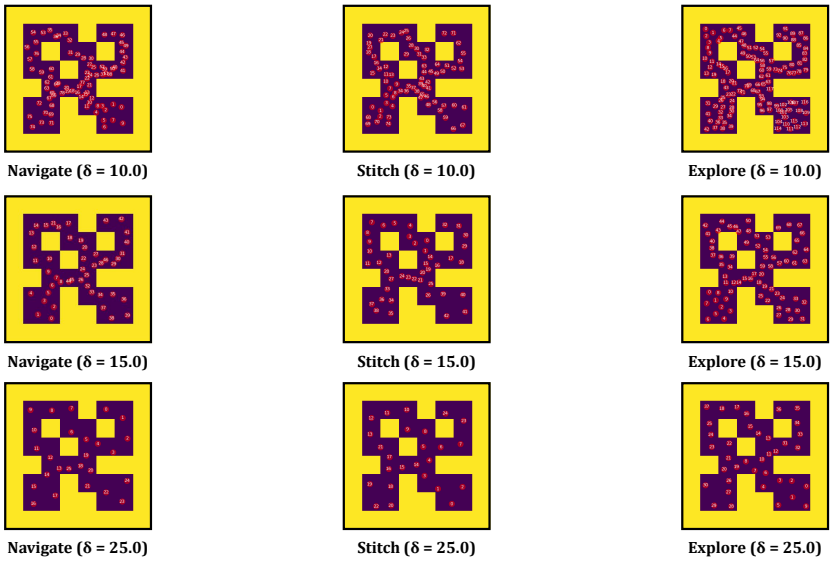

Figure 11: **OGBench :** Learned Mappings on **Medium Maze** according to the Dataset and the Repel Range (δ).

13.3 OGBench – AntMaze – Large

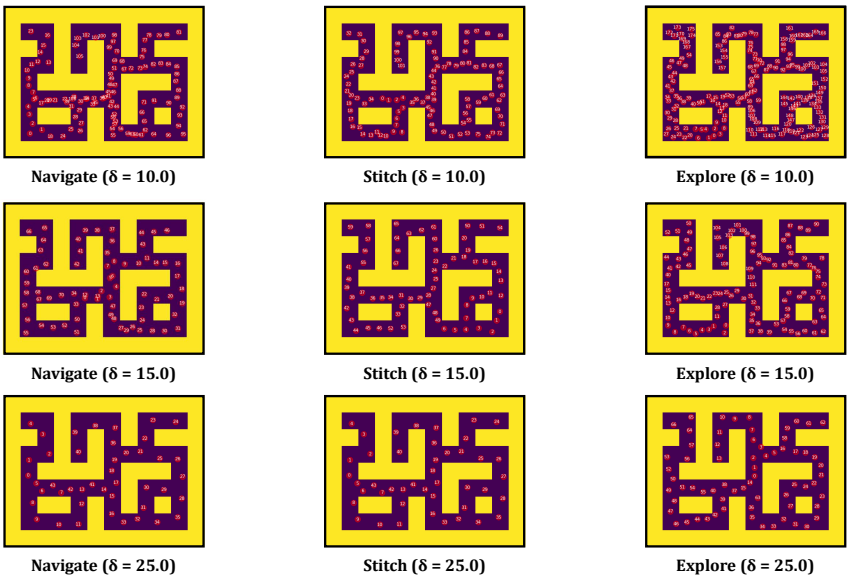

Figure 12: **OGBench :** Learned Mappings on **Large Maze** according to the Dataset and the Repel Range (δ).

13.4 OGBench – AntMaze – Giant

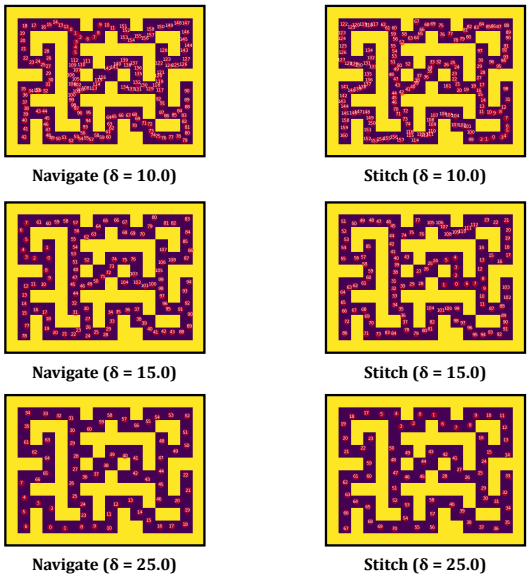

Figure 13: **OGBench :** Learned Mappings on **Giant Maze** according to the Dataset and the Repel Range (δ).

13.5 CONTINUAL NAVBENCH – AMAZEVILLE

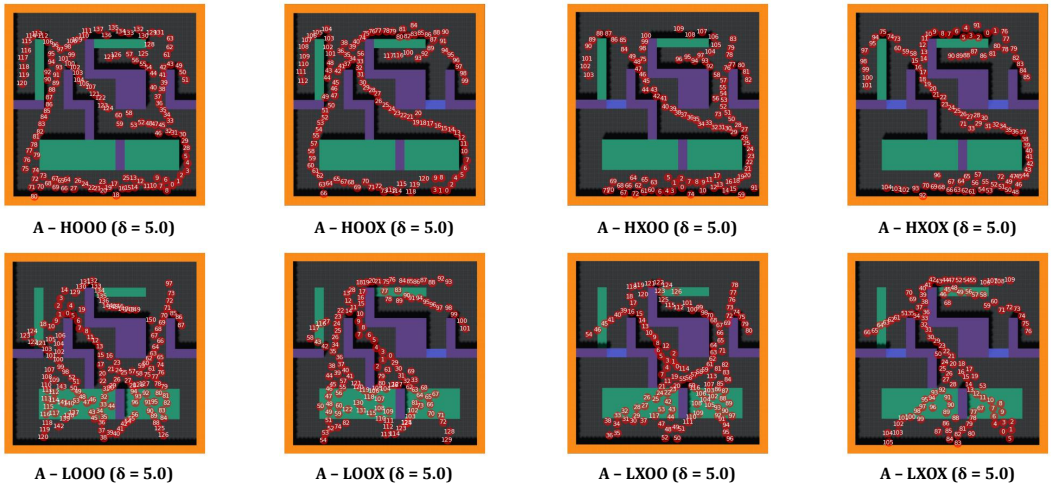

Figure 14: **Continual NavBench :** Learned Mappings on **AmazeVille** according to the Dataset and the Repel Range ($\delta = 5.0$).

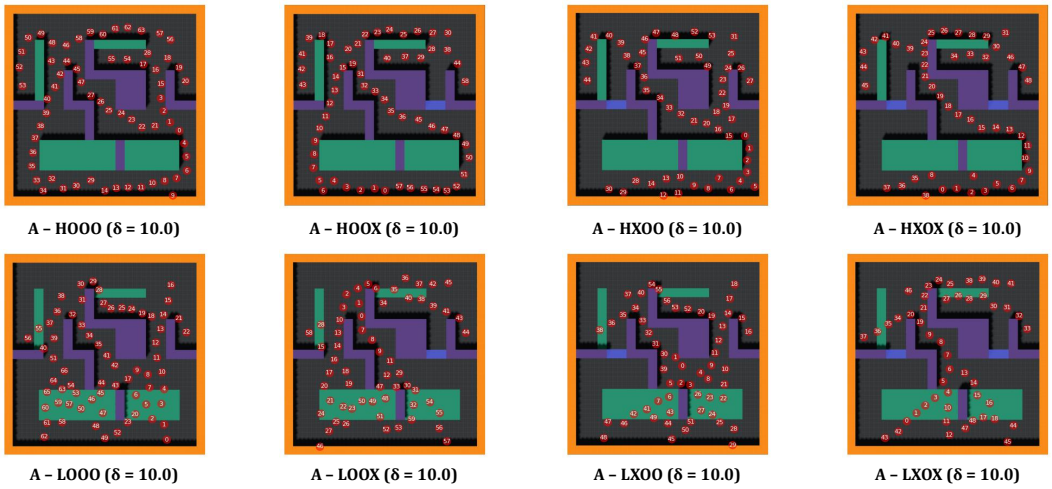

Figure 15: **Continual NavBench :** Learned Mappings on **AmazeVille** according to the Dataset and the Repel Range ($\delta = 10.0$).